Miniature Fiber-Optic Farby-Perot Interferometer: Fabrication, Data Processing and Temperature Sensing Application

A Dissertation

Presented to

the Faculty of the Department of Electrical and Computer Engineering

University of Houston

In Partial Fulfillment

of the Requirements for the Degree

Doctor of Philosophy

in Electrical Engineering

by

Zhihua Su

May 2013

Miniature Fiber-Optic Farby-Perot Interferometer: Fabrication, Data Processing and Temperature Sensing Application

Zhihua Su

Approved:

Chair of the Committee
Jiming Bao, Assistant Professor
Electrical and Computer Engineering

Committee Members:

Shin-Shem Steven Pei, Professor
Electrical and Computer Engineering

Han Q. Le, Professor
Electrical and Computer Engineering

Paul Ruchhoeft, Associate Professor
Electrical and Computer Engineering

Li Sun, Professor
Mechanical Engineering

Abdelhak Bensaoula, Research Professor
Physics

Suresh K. Khator, Associate Dean
Cullen College of Engineering

Badri Roysam, Professor and Chair
Electrical and Computer Engineering

Acknowledgements

First I would like to express deep gratitude to my advisor, Dr. Jiming Bao, for his continuous support, trust and invaluable help for my graduate study and research at the University of Houston. His solid background and broad experience in academic research is extremely valuable to me. I thank him for giving me a chance to work under his guidance and helping me build up my research skills. More importantly, he turned me into a more confident person by encouragement, productive discussion and determination. I am also grateful to all the committee members, Dr. Shin-Shem Steven Pei, Dr. Han Q. Le, Dr. Paul Ruchhoeft, Dr. Bensaoula Abdelhak, and Dr. Li Sun, for suggestions and help I received from them.

Special thanks go to Dr. Jian Gan for funding support on this project and all the creative suggestions. My gratitude also goes to Dr. Qingkai Yu, a great collaborator and friend. I benefit so much by working with him on many projects.

I want to thank all my colleagues and friends, specially Dr. Zhihong Liu, who was my mentor when I first came here. He contributed a lot on this research project. I would also like to thank Dr. Peng Peng and Dr. Wei Wu, who I have been closely working with on projects and learned a lot from. I want to thank my lab mates and good friends, Xiaoxiang Lu and Yanan Wang, who spent a lot of time with me on class and research projects. My gratitude also goes to Dr. Qiuhui Zhang and Zhuan Zhu who helped me a lot on this project, Dr. Longbiao Liao, Yang Li and Zhongzheng Zhao who were always available for help when I needed it.

Finally, my deepest gratitude and love goes to my family. I want to thank my parents, Xinnian Su and Qiaoyun Qin, for their protection when I was a child, for their

encouragement when I left home to study abroad, for their trust when I chose to pursue my Ph.D, and for their endless love that I can feel all the time. I want to thank my brother, Zhicong Su, who has been looking after me since I was young. I want to express my gratitude to my wife, Na Zhang, for her support, dedication and love. This work wouldn't be possible without her help.

Miniature Fiber-Optic Farby-Perot Interferometer: Fabrication, Data Processing and Temperature Sensing Application

An Abstract

of a

Dissertation

Presented to

the Faculty of the Department of Electrical and Computer Engineering

University of Houston

In Partial Fulfillment

of the Requirements for the Degree

Doctor of Philosophy

in Electrical Engineering

by

Zhihua Su

May 2013

Abstract

Temperature sensors are extremely important in academic research and industrial application. Among various temperature sensors, optical sensors are attractive due to many advantages. This dissertation focuses on the development of a robust optical temperature sensor with promising performance and a large measurement range.

Accuracy is the top concern for sensor applications. Previous study on FPI sensors shows noticeable hysteresis on temperature measurement. It can be attributed to ceramic glue in our experiment. An additional annealing is proposed for the sensor fabrication process, which can greatly reduce the hysteresis. The sensor performance before and after optimization is presented while significant improvement on hysteresis is obtained.

A generic novel data processing method is developed to accurately calculate the absolute optical path difference (OPD) of the FPI sensor cavity from broadband fringes. The method combines Fast Fourier Transformation (FFT) with non-linear curve fitting of the entire spectrum. The new method successfully resolves the ambiguous problem for the direct fitting method and can provide higher resolution compared to the FFT method.

Simulation on visibility shows that to achieve high visibility, careful control of the effective reflection coefficient is important. Fabry-Perot cavities with different effective reflection coefficient are synthesized, while the relationship between spectrum visibility and cavity length is plotted and compared with simulation results. A similar trend of visibility is observed, which indicates that visibility is related to the effective reflection coefficient and can be controlled by the fabrication process.

Extraction of additional phase is a challenge in this area, especially when cavity length is relatively small. In this dissertation a new method, which is based on the

difference of cavity length obtained from FFT method and curve fitting method, is proposed. In principle it can provide additional phase information even when the cavity length is small.

Table of Contents

List of Figures

Chapter 1: Introduction

1.1 Optical sensor

Optical sensors have attracted a lot of interest in a wide range of applications due to their robust performance. Among all kinds of optic sensors, fiber optic sensors are especially noticed and have shown great progress in the past several decades. They can be used for physical, chemical or biological parameter detection due to the interaction between these parameters and optical signal.

The measurement principle of fiber optic sensors can be extremely diversified, through which a larger number of sensor designs have been proposed. Besides numerous demonstrations and reports on fiber optic sensors in research laboratories, people are working on commercializing these sensors into industry because of incredible advantages over its electrical counterpart, including high flexibility, large measurement range and resistance to most chemical corrosion.

Among all the fiber optical sensors with different detection mechanisms, such as blackbody [1], Raman distribution [2], fiber grating [3-6], or interference based sensors [7-24] with silica [25], sapphire [15, 26, 27] or photonic crystal [12, 28] as sensor materials, interferometer configuration is believed to be suitable for weak signal detection because of high resolution. The operation mechanism of interferometers is usually based on two beam or multi beam interference which builds up spectral fringe for detection. The fringe pattern is directly related to the target parameter. Progress in research and application of interferometers [29] has been made with specified principle, such as Mach-Zender, Micholson or Fabry-Perot interferometer, the last of which is the focus of this research.

Fabry-Perot Interferometer (FPI) has significant advantage over other interferometers due to the immunity to polarization induced fading problem and its small size. For other interferometers mentioned above, one of the interfere arm is fully used as a sensitive element, while for FPI the sensitive element is the Fabry-Perot cavity whose size can be reduced significantly by fabrication technique. The small size of FPI can provide better spatial resolution for measurements, especially for temperature which usually has a large spatial distribution range in small area. People have demonstrated high performance of FPI sensor in temperature [10, 18], pressure [20, 30], strain [31, 32] and acoustic wave [8, 11] measurements.

1.2 Detail introduction to FPI sensor

FPI is named after the physicists Charles Fabry and Alfred Perot. It usually consists of two parallel-placed surfaces for light reflection. The interference fringe is generated by reflected light with constant OPD. Figure 1-1 is a schematic drawing of the Fabry-Perot cavity. In most FPI sensor designs, silica fiber is used and the reflection coefficient of fiber is relatively small. In this case, further reflection can be neglected because of low intensity. Reflected lights named R_1 and $R_{1,}$ which are obtained from first and second reflection surface, can generate an interference spectrum because they have same frequency and fixed OPD. The interference spectrum efficiently encodes cavity information which is sensitive to environment parameters.

Considering the traditional FPI, which builds up with two mirrors, fiber based FPI can provide features like small size and easy cavity alignment. Fiber based FPI can be classified into two types according to the behavior of incidental light, called intrinsic FPI and extrinsic FPI. In the extrinsic FPI, light can travel out of the fiber end and propagate

in other media (cavity material, most commonly air) before going back into incidental fiber, while in intrinsic FPI light would only propagate and be modulated inside incidental fiber.

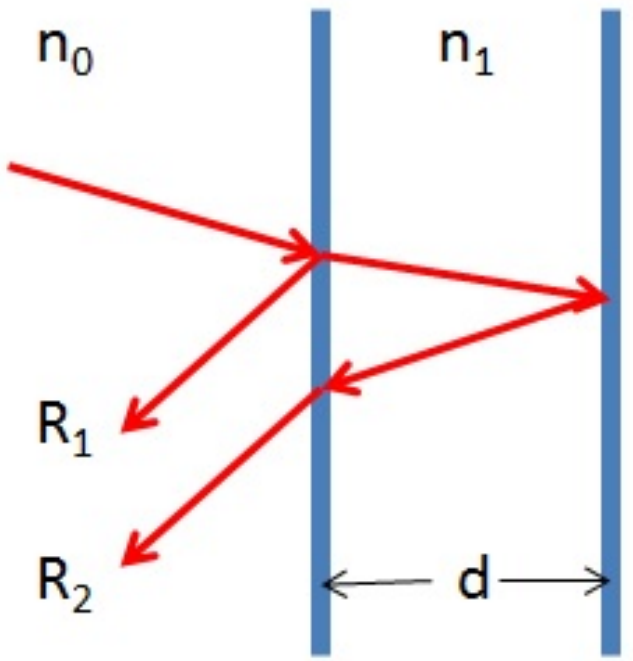

Figure 1-1: Schematic drawing of Fabry-Perot cavity

Intrinsic FPI has lower temperature resolution due to operation principle compared with extrinsic FPI. In order to obtain high resolution for intrinsic FPI, cavity material needs to be carefully chosen to assure clean interference spectrum with high signal to noise ratio. Figure 1-2 [13] shows the recent development on intrinsic FPI with reduced sensor size by directly fabricating a cavity on the fiber. It is as small as around 5 μm which is good for temperature measurement with ultra-high spatial resolution. Besides, the sole use of silica as sensing material also gives it an advantage on stability in harsh environments.

1.3 Motivation

Although research on intrinsic FPI is still in progress, people are paying more attention to the extrinsic FPI because of its advanced design and promised high resolution. Research progress has been reported on the development of extrinsic FPI, but fundamental problems still exist in this scientific area including hysteresis, accuracy, spectrum visibility and data processing.

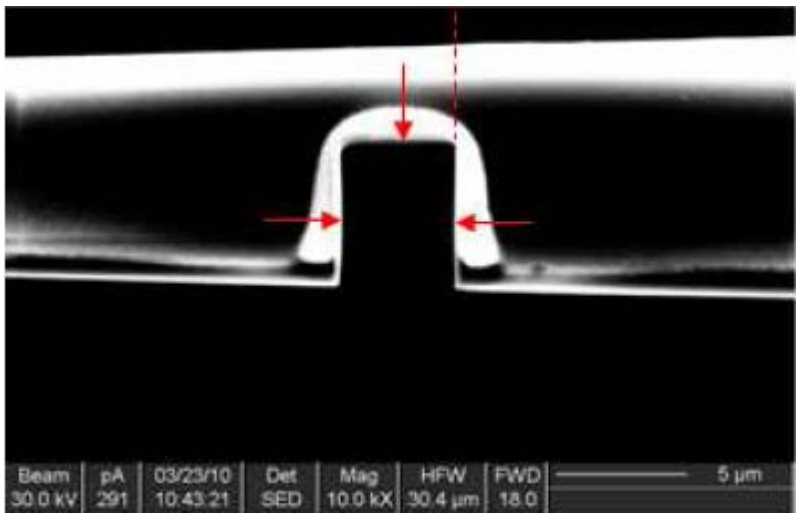

Figure 1-2: Recent development in Intrinsic FPI sensor

The motivation of this work is to fabricate temperature sensors which can survive in harsh environments for a long time with excellent performance. Fabrication optimization is necessary to reduce the hysteresis problem. Improvement on data processing techniques is required to resolve ambiguity problem and provide high resolution temperature extraction. Critical challenges in performance of extrinsic FPI are addressed, while a high quality, robust FPI sensor is demonstrated in temperature sensing applications with measurement ranges from room temperature to as high as 850 °C.

1.4 Scope of dissertation

1) Achieve the best design of FPI to meet large measurement range, small size and high accuracy measurement requirement
2) Optimization of fabrication process to reduce hysteresis that has been reported and improves sensor stability
3) Long-term high temperature stability test, to make sure sensor can survive in harsh environments
4) Improve data processing techniques to resolve the ambiguous problem and acquire high temperature resolution
5) Study spectrum visibility for sensor quality control
6) Extract additional phase information from measured spectrum

A detailed background on FPI will be given below, while basic FPI theory is discussed in chapter 2. Sensors with different designs are discussed and compared in chapter 3, in which the best design is obtained. In chapter 4 sensor fabrication process is presented, along with a comparison between sensor performance before and after the optimization process. A novel data processing technique is proposed and discussed in chapter 5 which shows advantages over the previous methods. Chapter 6 focuses on the visibility simulation of FPI sensor, specially the relationship between visibility and effective reflection coefficient of cavity surface. Detailed comparison between the simulation and experimental results on visibility of spectrum is given in chapter 7, with a proposed method to improve spectrum visibility. The additional phase is discussed in chapter 8, and a novel technique to extract additional phase information for small cavity length which is still challenging to present data processing techniques is proposed. Detail

discussion on sensor calibration, long-term stability, product specification and multiple sensor system build up is given in chapter 9.

1.5 Detail background

The focus of this research is fiber optic sensors. Traditional temperature sensors which use the electrical signals as measurement element will not be discussed.

As previously mentioned, FPI has been widely studied for over 20 years. Based on the cavity design, it can be classified into intrinsic or extrinsic FPI. Besides that, it can also be classified into silica fiber based or sapphire fiber based FPI according to cavity materials, which gives different temperature measurement ranges because sapphire has higher temperature tolerance.

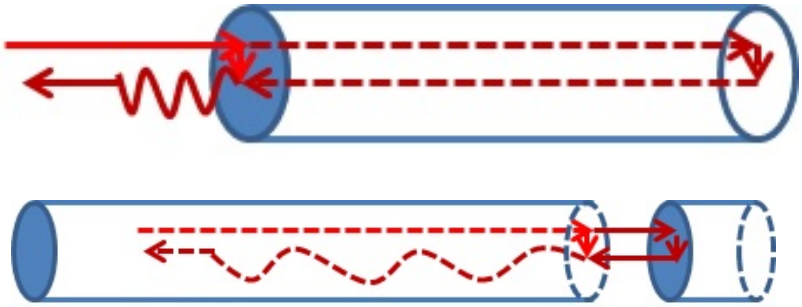

Figure 1-3: Schematic drawing of Intrinsic (top) and extrinsic (bottom) FPI

Two parallel placed surfaces are required for a FPI cavity. Various designs on intrinsic FPI have been proposed, including micro-window fabrication on fiber [13], wafer based FPI [19, 23], or fused fiber segment with two plane surfaces. Extrinsic FPI usually has an air gap cavity. In fiber based extrinsic FPI, the air gap cavity is formed by two plane surfaces from different fibers. One surface is on a fiber segment, while the other surface is usually on a lead-in fiber which can also be used as light guider. Figure 1-3 shows schematic drawing of intrinsic and extrinsic FPI for comparison. In extrinsic FPI, the fiber segment may sometimes be replaced by small mirror in a slightly alternate

design. For expansion tube design, the two fibers are confined in an expansion tube to obtain good surface alignment. The material of the tube is usually different from fiber and has a large thermal expansion coefficient for high temperature resolution if the FPI is used as temperature sensor.

The above discussion is focused on temperature sensors. For pressure or acoustic wave sensors, the fiber segment is usually replaced with displacement sensitive film.

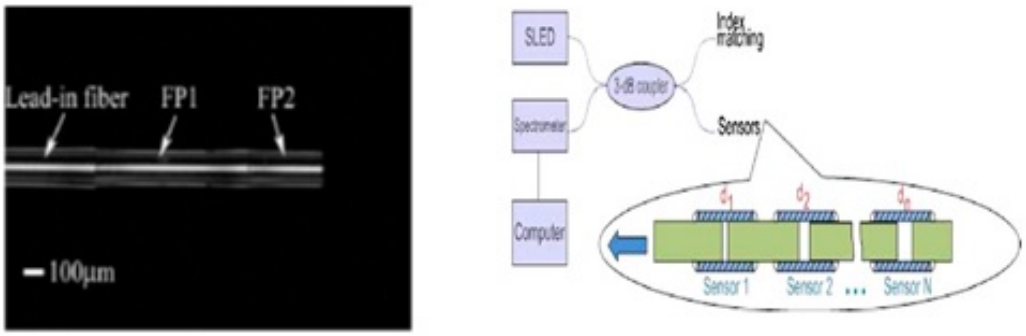

Figure 1-4: multi detection system for intrinsic (left) and extrinsic (right) FPI

Besides basic FPI setup, people have also developed a multiple FPI detection system, in which FPI sensors are connected in a series. Figure 1-4 [15, 33] shows multiple sensor systems for both intrinsic and extrinsic FPI design. The In-line multiple sensor system requires better data processing techniques for information extraction because of multiple interference.

Sapphire fiber has a high melting point, which makes it useful in high temperature measurement. However, sapphire fiber costs more compared with silica fiber and requires signal coupling when connecting into commercial optical systems.

Silica fiber has a relatively low melting point which makes it useless when the desired temperature measurement range is beyond 1000 ^{o}C. Besides that, silica fiber based FPI has many advantages, including ease of fabrication, high resolution and

compatibility with many components that have been used in well-established optical fiber systems. People can use single mode silica fiber (SMF) or multimode silica fiber (MMF) as cavity material. Single mode fiber is commercially used in various areas. Signal to noise ratio for single mode fiber is better than multimode fiber. Besides, data processing techniques of multimode fiber are more complex and require additional effort. In this research, single mode fiber based FPI and multimode fiber based FPI will both be fabricated, and performance of them will be compared for best design.

Chapter 2: FPI theory

2.1 Fabry-Perot interference

Figure 2-1 shows a schematic drawing of a Fabry-Perot cavity with perpendicular incidental light for better understanding of FPI sensor. A Fabry-Perot cavity simply consists of two reflection surfaces which are placed parallel to each other. Light guided into the system will be partially reflected by the first surface, while residual transmitted light will propagate through the cavity and be reflected by the second surface. The two reflected beams propagating in reverse direction to incidental light will generate interference which actually introduces intensity peak or valley depending on the wavelength of incident light and OPD. If light comes from a broad band light source, the spectrum of reflected light will exhibit fringe pattern. Since the reflected coefficient of two surfaces is small, further reflection from the cavity can be ignored.

The portion of reflected light mainly depends on the reflection coefficient and surface condition of cavity material. Although the reflected light from first surface and total reflected light from FPI can be readily monitored and recorded by spectrometer, it is not quite convenient to record light introduced by the second surface. Usually reflected light from first surface is fixed once the FPI is formed, but the intensity of light from the second surface can change when cavity length changes. As will be discussed, the spectrum visibility, which can be used to evaluate the quality of FPI sensors, is highly dependent on the intensity of two beams. So it is important to carefully control the intensity of two beams to obtain high quality FPI.

The fringe density of the interference spectrum greatly depends on the OPD of two beams which is solely determined by Fabry-Perot cavity. Cavity length, which is

sensitive element to environment, can be affected by temperature, strain or pressure, as discussed previously. By data processing, the interference spectrum can be used to extract cavity information and further to obtain environment parameters like temperature. FPI with low reflection coefficient material is called low finesse FPI. In our case, silica fiber or glass disk is used to build up a cavity in most case. The reflection coefficient of typical silica fiber is 0.04, which makes our sensor perfect as low-finesse FPI. Although intensity of reflected light is mainly controlled by material properties, the surface roughness and alignment can also play a role and contribute to effective reflection coefficient. By using the same material and controlling the surface condition, high quality interference patterns can be achieved.

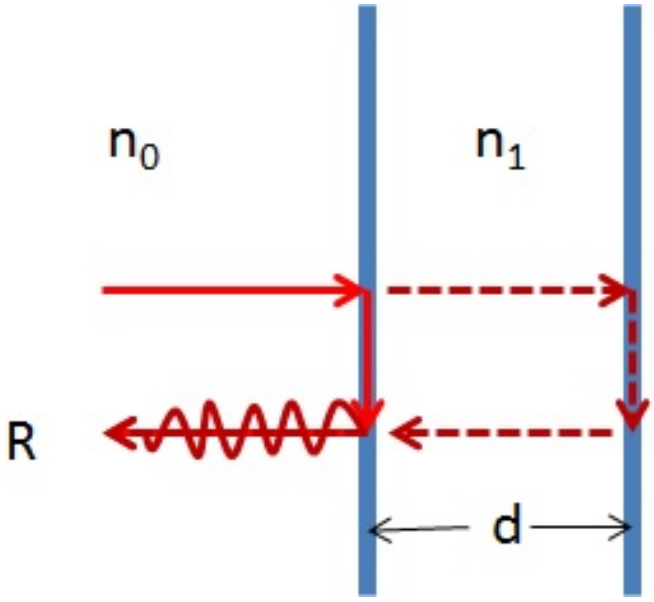

Figure 2-1: schematic drawing of F-P cavity with perpendicular incident light

A simple analysis of FPI was given by Murphy [17]. It was mainly based on two-beam interference, while reflected lights from two parallel surfaces are assumed to be plane wave.

Assume we have incidental light described by the following Equation,

$$I = I_0(\lambda) = |E_0(\lambda)|^2, \tag{2.1}$$

where λ is wavelength. The reflected light from first surface is given by,

$$E_1 = E_0 * \sqrt{B} * e^{i(kx-wt)}. \tag{2.2}$$

The reflected light from the second surface can be given by,

$$E_2 = E_0 * (1-B) * \sqrt{D} * e^{i(kx-wt)} * e^{i\pi} * e^{i(\frac{4\pi l}{\lambda})}, \tag{2.3}$$

where B is the effective reflection coefficient of the first surface and D is the effective reflection coefficient (the reason why we use effective reflection coefficient is because light reflected by two surfaces can be affected by surface condition of fiber) of the second surface, L is cavity length. $e^{i\pi}$ is phase term caused by half wave loss when light travels from low density media to high density media.

Here we use plane wave to represent the two reflected lights. It is a good assumption for most data processing, while in reality a small modification on this model will be necessary.

Also we assume there is no loss during light propagation inside and outside the cavity. Then the intensity of total reflected light measured by spectrometer can be given as,

$$I_f = I_0 * [B + (1-B)^2 * D + 2 * (1-B) * \sqrt{B * D} * \cos(\frac{4\pi l}{\lambda} + \pi)]. \tag{2.4}$$

By simplifying of above Equation, we can get,

$$I_f = I_0^{'} * (1 + A\cos(\frac{4\pi L}{\lambda} + \pi)). \tag{2.5}$$

While we have the following Equation for parameter details,

$$I_0^{'} = I_0 * (B + (1-B)^2 * D), \tag{2.6}$$

$$A = \frac{2*(1-B)*\sqrt{B*D}}{B+(1-B)^2*D}. \quad (2.7)$$

In case B and D are small and equal, we have,

$$I_f = I_0^{'} * (1+\cos(\frac{4\pi L}{\lambda}+\pi)) = I_f(\lambda, L), \quad (2.8)$$

where I_f is reflection spectrum, L is cavity length, λ is light wavelength. The above Equation shows that measured light intensity is a function of wavelength and cavity length for a fixed light source and plane wave interference.

Cavity length is encoded in interference fringe, so it is possible to extract cavity length L by data processing techniques.

It should be noticed that in the above discussion we use an assumption that light propagating inside fiber and cavity is plane wave. In reality, light propagated inside the fiber usually has Gaussian distribution and will expand. The above assumption is good for most data processing and detection applications.

2.2 Temperature detection mechanism

Cavity length L is a sensitive element. For temperature measurement, detection mechanism of FPI is based on thermal expansion of material. Temperature can cause a change of cavity length, which will cause a shift of spectrum. Intrinsic FPI and extrinsic FPI have different responses to thermal expansion and will be discussed separately below.

For Intrinsic FPI as shown in Figure 1-3, the relationship between temperature and cavity length can be described by the following Equation,

$$L = L(T) = L(T_0) + L(T_0) * k * \Delta T = L(T_0) + \Delta L, \quad (2.9)$$

where k is the thermal expansion coefficient of cavity material and the change of cavity length can be given by,

$$\Delta L = L(T_0) * k * \Delta T. \tag{2.10}$$

For extrinsic FPI, the relationship between temperature and cavity length is more complicated which is given in Equation below,

$$L = L(T) = L(T_0) + D * k_1 * \Delta T - (D - L(T_0)) * k_2 * \Delta T = L(T_0) + \Delta L, \tag{2.11}$$

where k_1 is the thermal expansion coefficient of the ceramic tube (material 1), k_2 is the thermal expansion coefficient of the fiber (material 2), D is the length of the ceramic tube, and we have,

$$\Delta L = D * k_1 * \Delta T - (D - L(T_0)) * k_2 * \Delta T = D * (k_1 - k_2) * \Delta T + L(T_0) * k_2 * \Delta T. \tag{2.12}$$

As discussed before, a change of cavity length will cause a shift of interference fringe, either to a longer wavelength for increase of cavity length or to a shorter wavelength for decrease of cavity length. Fringe density will also change. High fringe density is from large cavity length interference while low fringe density is from small cavity length interference. We can directly monitor cavity length difference by observation of fringe shift or density. If we keep monitoring one interference peak located at wavelength λ and ignore half wave loss which is not critical in the following discussions, we have,

$$\frac{2L}{\lambda} = n, \tag{2.13}$$

$$\frac{2(L + \Delta L)}{\lambda + \Delta\lambda} = n, \tag{2.14}$$

where n is the interference order for fringe peak at wavelength λ. By substituting n into Equation 2.14, we get,

$$2\Delta L = n\Delta\lambda. \tag{2.15}$$

By solving the above Equation with intrinsic FPI and extrinsic FPI, we obtain the temperature response for intrinsic FPI and extrinsic FPI,

$$R_i = \frac{\Delta\lambda}{\Delta T} = k * \lambda, \tag{2.16}$$

$$R_e = \frac{\Delta\lambda}{\Delta T} = \frac{D*(k_1 - k_2)*\lambda}{L(T_0)} + k_2 * \lambda. \tag{2.17}$$

Conclusions can be achieved based on the above discussion. For intrinsic FPI, the temperature response is only related to spectrum wavelength and thermal expansion coefficient of material. For extrinsic FPI, it is not only related to the thermal expansion coefficient of materials, but also affected by sensor designs. It is possible to achieve high temperature response compared to intrinsic FPI by changing of D and $L(T_0)$. If D is much larger than $L(T_0)$, temperature response can be improved by 50 or more times. Better temperature response usually means higher temperature resolution.

2.3 Brief discussion on interference pattern

Fringe visibility of interference spectrum is defined as following Equation,

$$F = \frac{I_{\max} - I_{\min}}{I_{\max} + I_{\min}}, \tag{2.18}$$

where $I_{\max}$ and $I_{\min}$ are maximum and minimum of interference fringe. Figure 2-2 shows the typical interference spectrum.

Visibility is important for data processing and can be used to evaluate sensor quality. It is determined by wavelength, cavity length, cavity material and surface condition.

In reality, if we use extrinsic FPI design, we have to consider how light propagates inside the cavity. It is related to discussion on visibility, coupling efficiency and an additional phase term, which will be given in other chapters.

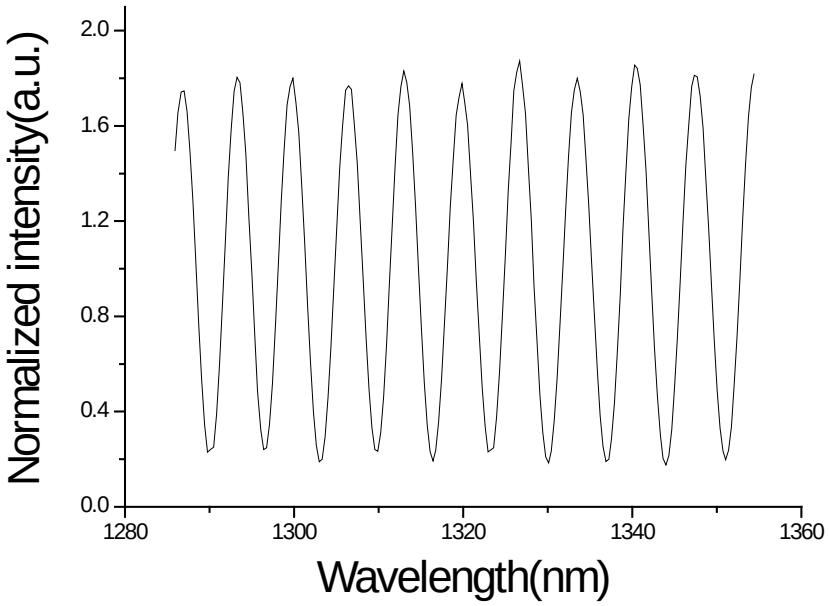

Figure 2-2: typical interference spectrum after removal of background

Chapter 3: Comparison of different FPI design

Sensor quality, which includes accuracy, temperature resolution, measurement range and stability, is the main concern of sensor design. While extrinsic FPI has an advantage in temperature resolution, intrinsic FPI is usually more stable and easy to fabricate. Unless we compare the sensor performance based on different designs, it is hard to tell which one is the best choice in our application.

Spectrum quality, including visibility and signal to noise ratio, is another important factor in sensor application due to its effect on data processing and accuracy of temperature measurement. Different sensor designs can bring different spectrum quality. To obtain the best design for our application, sensor performance is compared and given below.

3.1 Intrinsic FPI with sapphire disk cavity

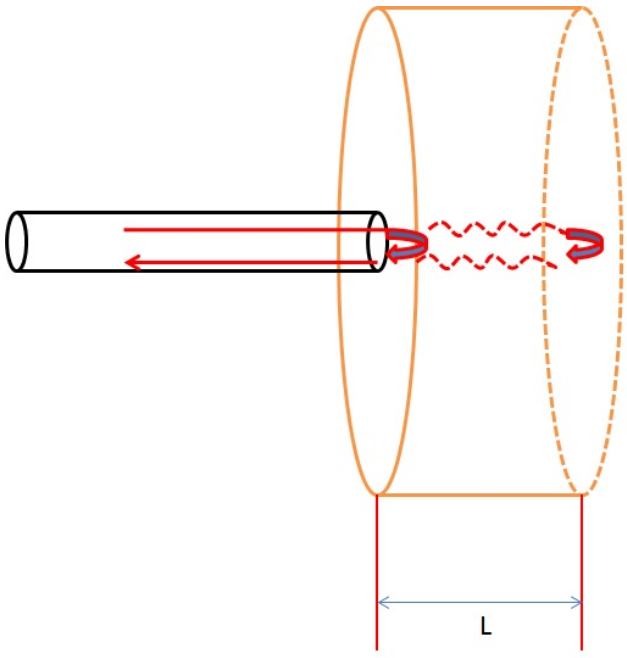

Figure 3-1: Schematic of sapphire disk cavity design

A white light source is used in this setup. We use a multimode fiber to guide the light into the sapphire cavity. The thickness of the sapphire disk is around 100-300 um at room temperature. The spectrometer we used is Ocean Optics HR2000+, with a measurement range from 760nm to 940nm.

Figure 3-1 shows a schematic drawing of sensor design. Ceramic glue is used to bond the fiber end to the sapphire disk. We achieved the interference pattern from this setup and recorded temperature measurement data for analysis.

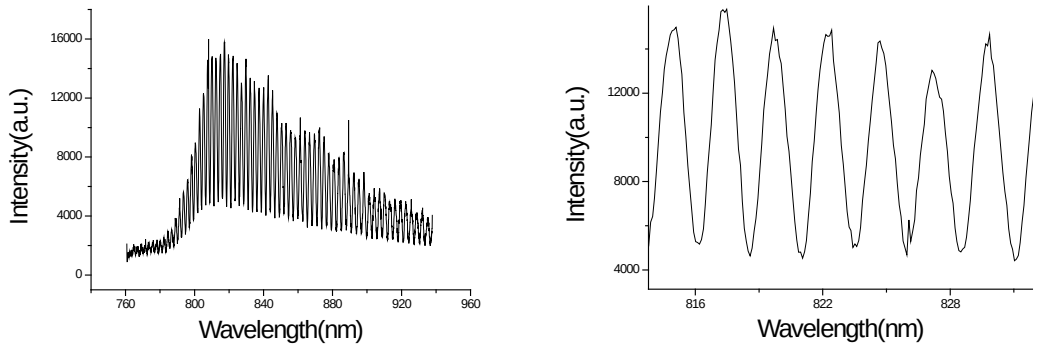

Figure3-2: Room temperature interference pattern

Figure 3-2 shows the room temperature interference pattern of the sapphire disk based FPI sensor. It has high density fringe which is not very good for data processing. Fringe density is mainly determined by the wavelength range of the light source and thickness of cavity. To reduce fringe density, a thin sapphire disk should be used. The calculation based on the two-peak method which will be discussed in detail, provides rough thickness evaluation of about 136 μm. This is intrinsic FPI design and has low temperature resolution, which is confirmed by temperature measurement results.

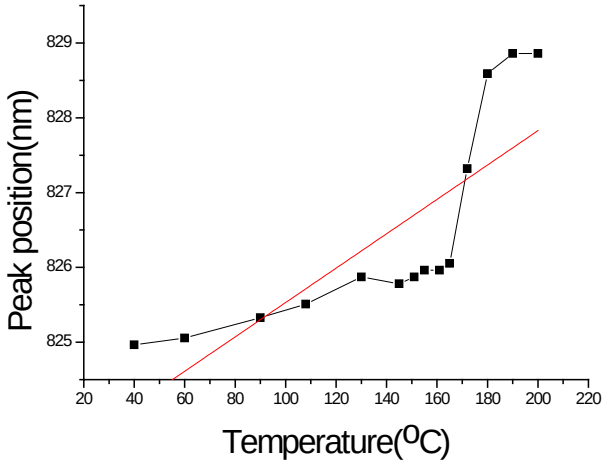

Figure 3-3: Using sapphire disk based temperature sensor to measure temperature

Figure 3-3 shows temperature sensing performance. As predicted, the interference pattern shifted to longer wavelength due to thermal expansion of cavity length when temperature increased. This conclusion is reached by tracking of one peak that originated at around 824nm at room temperature. We found that temperature change of about 200 ^{o}C can only cause spectrum shift of around 4nm, which makes temperature response less than 50^{o}C/nm. Although we have a high resolution spectrometer, the sensor performance is still not promising. It should also be noticed that the visibility and signal to noise ratio of this spectrum is not exceptional. Besides, it is hard to fabricate a small sensor based on sapphire disk design. Based on above discussion, we believe that although sapphire disk cavity can provide high temperature tolerance, the intrinsic design and low spectrum qualify makes it useless in our application.

3.2 Extrinsic FPI, with fiber-glass cavity

As discussed and demonstrated before, the temperature response of intrinsic FPI is not promising for our application. To improve it, we tried extrinsic FPI setup. The end surface of a multimode fiber is used, together with the surface of a glass disk, to build up

a Fabry-Perot cavity. The multimode fiber is confined in a ceramic tube to assure alignment with the surface of the glass disk. Here we can readily replace the glass disk with the sapphire disk to improve temperature tolerance.

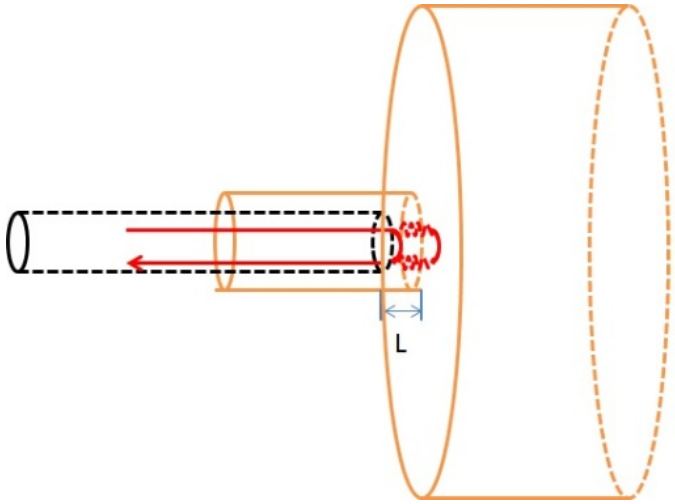

Figure 3-4: Schematic drawing of fiber-glass disk cavity

Figure 3-4 shows a schematic drawing of this setup. Ceramic glue is used to bond the ceramic tube to the fiber and glass disk. The Interference pattern at room temperature is obtained and shown in Figure 3-5. Fringe density is lower compared to sapphire disk based intrinsic FPI, because the distance between the fiber end and glass disk is controlled. With a similar calculation approach, the corresponding cavity length is roughly evaluated to about 40μm. The theoretical temperature response of this setup is improved, but signal quality here decreases significantly. We believe it is mainly due to the white light source and multimode fiber. Besides, using a glass disk as the second reflection surface still makes the sensor size large compared to the traditional thermal meter. Reducing the disk size can cause difficulty of operation for alignment.

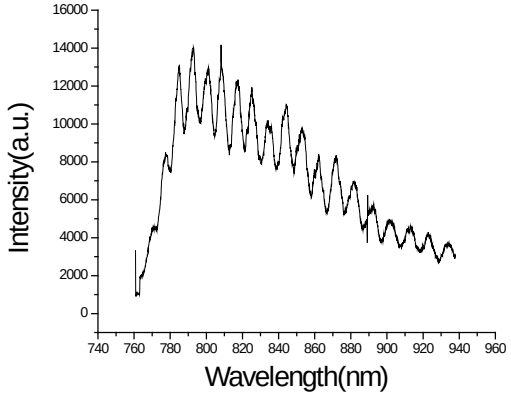

Figure 3-5: Room temperature interference pattern

3.3 Extrinsic FPI, multimode fiber, fiber-fiber cavity

To reduce the sensor size, we tried another design which uses a fiber-fiber cavity with multimode fiber and white light source. Compared with the previous design, it significantly reduces sensor size. However, the spectrum quality of this design is still low. Figure 3-6 shows the interference spectrum. It is hard to obtain cavity information from data with such a low signal to noise ratio. Fiber polish can actually improve the spectrum quality. However, even after improvement, spectrum quality is still low for data processing, as shown in the right hand image of Figure 3-6.

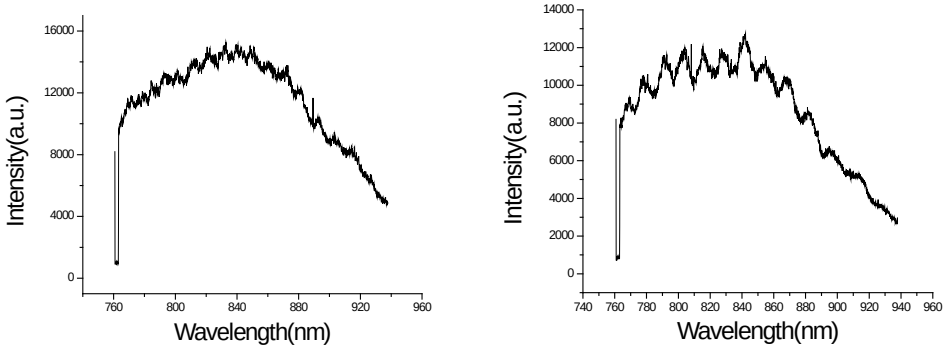

Figure 3-6: Room temperature interference pattern by multi-mode cavity, using direct cleave fiber (left) and polishing fiber (right)

3.4 Extrinsic FPI, Single mode fiber, fiber-fiber cavity

We believe that while light and multimode fiber can affect the singnal to noise ratio of the spectrum, which then further decreases sensor quality and causes difficulty in data processing. A fiber to fiber cavity end can reduce the sensor size, which is an advantage in sensor design. Besides, commercially used single mode fibers with a diameter of 125 um can reduce the cost and provide easy integration into full light communication systems. Based on the above discussion, we tried fiber-fiber cavity design with an infra-red light source and single mode fiber. Figure 3-7 shows typical interference pattern at room temperature obtained from this design. The initial cavity length can be controlled during the fabrication process. The fringe is clean and smooth in this spectrum. The light source we used here has Gaussian shape and can be easily removed for data processing. Detail analysis will be given in other chapter.

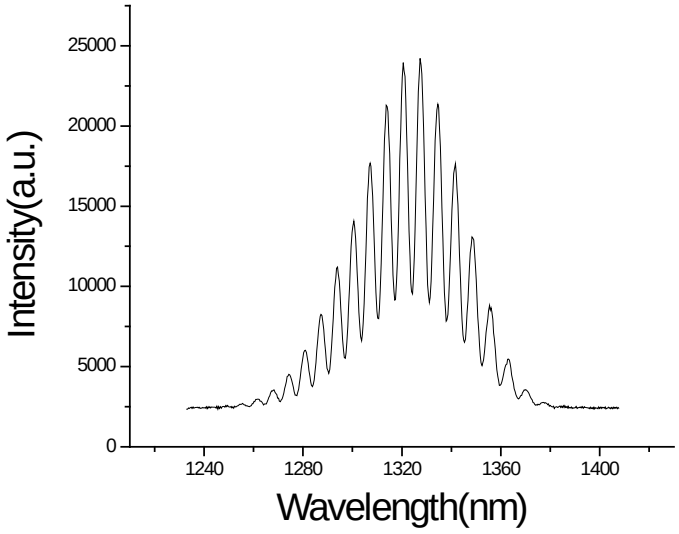

Figure3-7: Room temperature interference pattern by single-mode cavity

3.5 Detail discussion on single mode fiber based FPI

As discussed above, the final design for our FPI temperature sensor is using Fiber-Fiber cavity and super luminance diode as a light source with the center wavelength located at 1310 nm. The spectrometer we used for this setup is Ocean Optics NIR 512, which gives us high wavelength resolution from around 1240 nm to 1400 nm. Full width half maximum (FWHM) of light source is around 50 nm. It is enough for data processing. The peak position of the light source will shift slightly when changing the output power.

To develop the temperature measurement system, a single mode fiber coupler is used. The schematic drawing of system is given in Figure 3-8. Incidental light goes through the fiber coupler and reaches FPI, then gets reflected. Reflected light goes back to the coupler and partially reaches the spectrometer. The recorded spectrum is used for analysis and data processing by computer. Details of sensor design are also given in the schematic drawing. The fiber coupler has 50/50 light splitting capability.

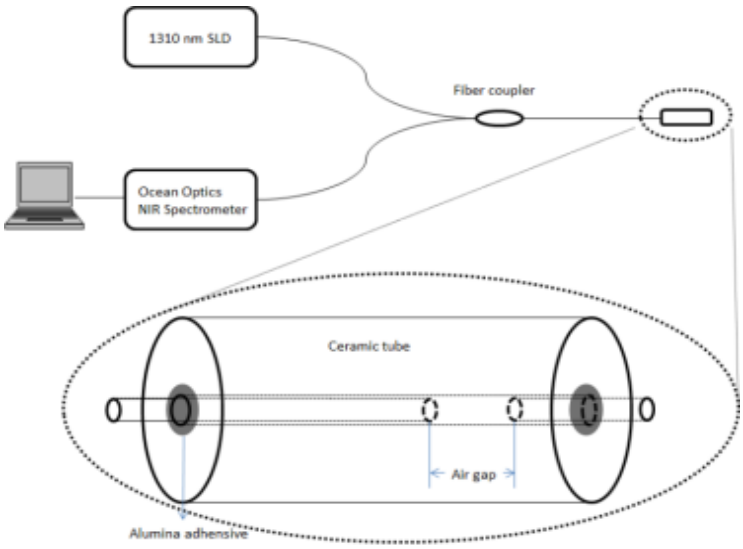

Figure 3-8: schematic drawing of temperature sensing system

The fiber is bonded to the end of the ceramic tube by ceramic glue. The diameter of the fiber is 125 um, including both core and cladding. The inner diameter of the ceramic

tube is about 127 um, with size deviation of about 5-50 μm. Although for some ceramic tubes, the confinement for the fiber inside the tube is not tight, we can always obtain high spectrum quality by adjusting fiber position with 3D stage.

Based on the above design, we fabricate FPI sensors with different room temperature cavity lengths. Figure 3-9 shows three typical interference spectrums obtained from three sensors. The black curve shows the interference from the smallest cavity length, while the blue curve shows the interference spectrum from the largest one. All three spectrums show good signal to noise ratio and high visibility. By the two-peak method, we can obtain a rough guess on the cavity length of these three sensors: 28um for black curve, 124um for red curve and 144 um for blue curve. We can control the room temperature cavity length by observation of interference spectrum during fabrication (different data processing techniques will be discussed) .

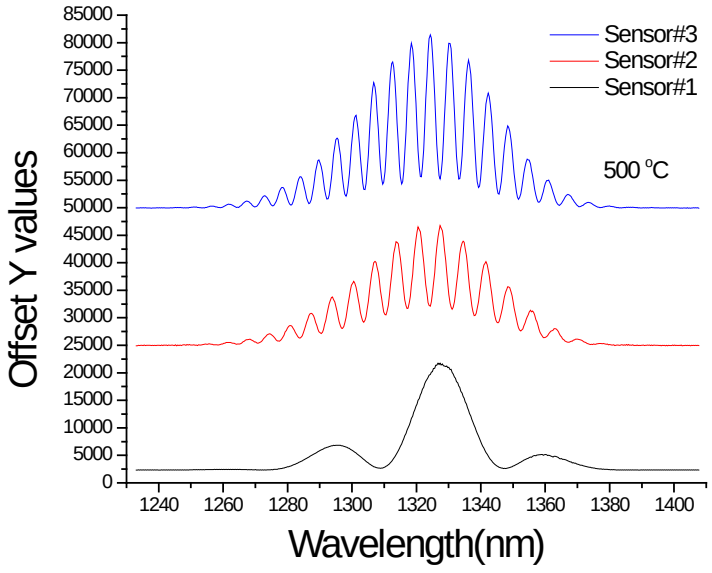

Figure 3-9: Interference spectrums from typical FPI

Figure 3-10 shows the actual FPI sensor that is fabricated using a ceramic tube and single mode fiber. The length of the sensor is around 5 mm, while the diameter is less

than 1 mm. One end of the sensor is a fiber segment bonded to the ceramic tube. The length of fiber outside the ceramic tube can be controlled depending on the application and operation requirements. The other end of the sensor is connected with the fiber coupler, which is used as both light guider and cavity surface.

Figure 3-10: Actual fabricated FPI sensor tip

3.6 Interference pattern shift in response to small temperature change

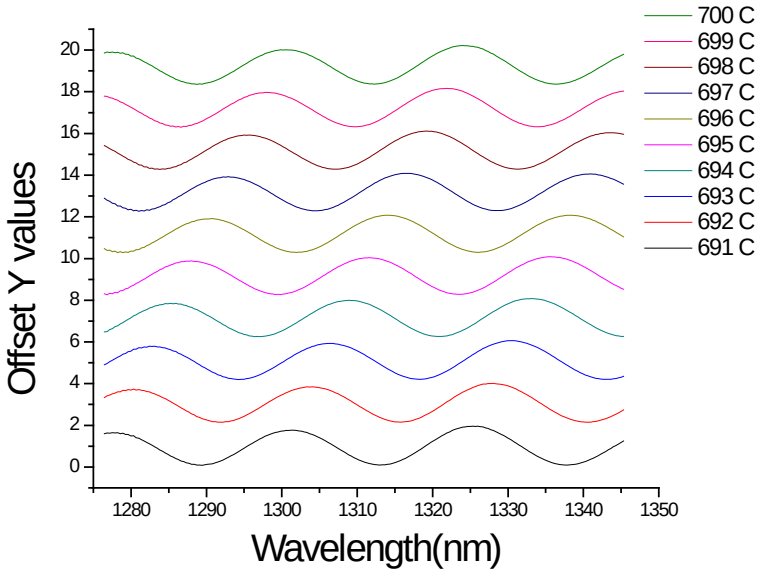

Figure 3-11: Peak shift as function of temperature

After sensor fabrication, we performed an initial test of sensor response to temperature. We heat the sensor to about 700 ^{o}C. The spectrum from 690 ^{o}C to 700 ^{o}C with 1 ^{o}C step is recorded and shown in Figure 3-11.

A clear peak shift to larger wavelength is observed with the increase of temperature. Shift rate is about 2 nm/ ^{o}C, which is 100 times larger compared to intrinsic FPI discussed above with about 0.02 nm/ ^{o}C shift rate. To better show the sensor response, we draw the cavity length of the sensor as a function of temperature, given in Figure 3-12. It shows a linear relationship. That is because change of cavity length is mainly determined by initial cavity length and the thermal expansion coefficient of fiber material according to the previous discussion. In a small temperature range, the thermal expansion coefficient of the ceramic tube and fiber does not change much, and the change of cavity length will follow a linear relationship. It is easy to imagine that in a large temperature range like from room temperature to 700 ^{o}C, the thermal expansion coefficient cannot keep same value.

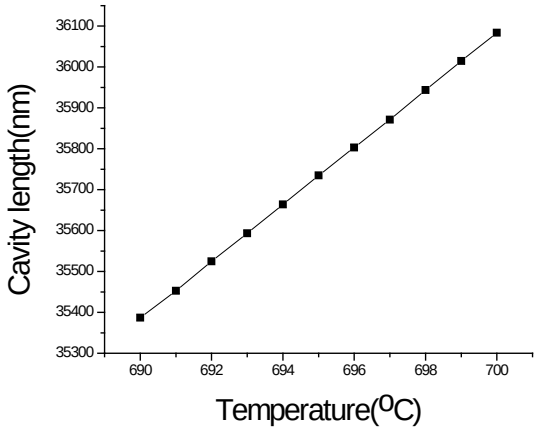

Figure 3-12: cavity length as function of temperature

This method can provide an alternate way for determination of the thermal expansion coefficient of materials at different temperatures.

Chapter 4: Sensor fabrication and optimization

4.1 Sensor fabrication

The material we used for FPI fabrication mainly consists of fiber segments and a ceramic tube. To build up the whole system, we also need a light source, spectrometer and fiber coupler. As discussed before, the light source we used is a broadband Super Luminescent Diode, with the wavelength centered at 1310 nm. The spectrometer we used is NIRQuest 512 from Ocean Optics, with 0.34 nm spectrum resolution and a spectrum range from 1233nm to 1407.69 nm. The fiber coupler is a commercially used single mode fiber coupler with around 10 um core diameter. The light source provides us a Gaussian like spectrum, with FWHM of around 34 nm. The peak position and FWHM of the light source can be affected by the output power, but the difference is not significant in our application.

Step 1: Prepare fiber segment

Figure 4-1: optical image of fiber polisher and polished fiber surface

The previous discussion shows that we need two parallel surfaces to build up the cavity. The two surfaces are obtained on fiber ends. One of them is on a fiber segment, while the other is on the leading fiber. So first we need to have a fiber segment with a

length longer than half the length of the ceramic tube, which is 3 mm. Then we need to prepare a plane and smooth surface on the end of the fiber segment. Different methods including cleaving and polishing have been tried. Although the fiber polishing method can provide a perfect surface, it takes a lot longer compared with the cleaving method. Figure 4-1 shows the fiber polishing tools we used and the fiber end after polishing.

The polishing of the fiber can be done both by hand and with the polisher. To polish fiber with a polisher, we designed the fiber holder, which can be mounted onto the polishing tool shown in Figure 4-1. The reason why we need a fiber holder is because the fiber is fragile and could easily be broken during polishing, especially when a larger force is applied tangential to the fiber axis direction.

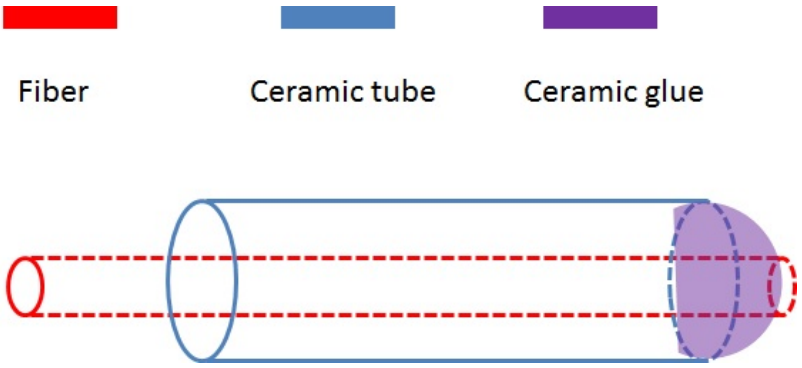

Figure 4-2: Schematic drawing of fiber holder

We first guide the fiber into a glass tube with an inner diameter around 500 um, making sure that the fiber end is outside the glass tube with about 0.5mm length, as given in schematic Figure 4-2.

Then we use molten epoxy glue to bond the fiber to the glass tube, while the fiber end is covered with the glue. The glass tube can be easily clipped by the polisher tool, with the fiber end protected by epoxy glue from being broken by applied force. The

results show that a promising surface is obtained as given in Figure 4-1. We also tried fiber cleaving approach. It saves a lot of time and surface condition is acceptable.

Step 2: Align fiber segment in to ceramic tube

To build up the Fabry-Perot cavity, we need to carefully guide the fiber segment into the ceramic tube. A 3D stage is used in this step. The ceramic tube is firstly fixed on the table. Then the fiber segment is attached on the 3D stage and carefully guided into one pore of the ceramic tube. There are two pores for each ceramic tube, with pore diameter around 127 um with relative tolerance. The length of fiber segment inside the ceramic tube can be roughly controlled by the 3D stage.

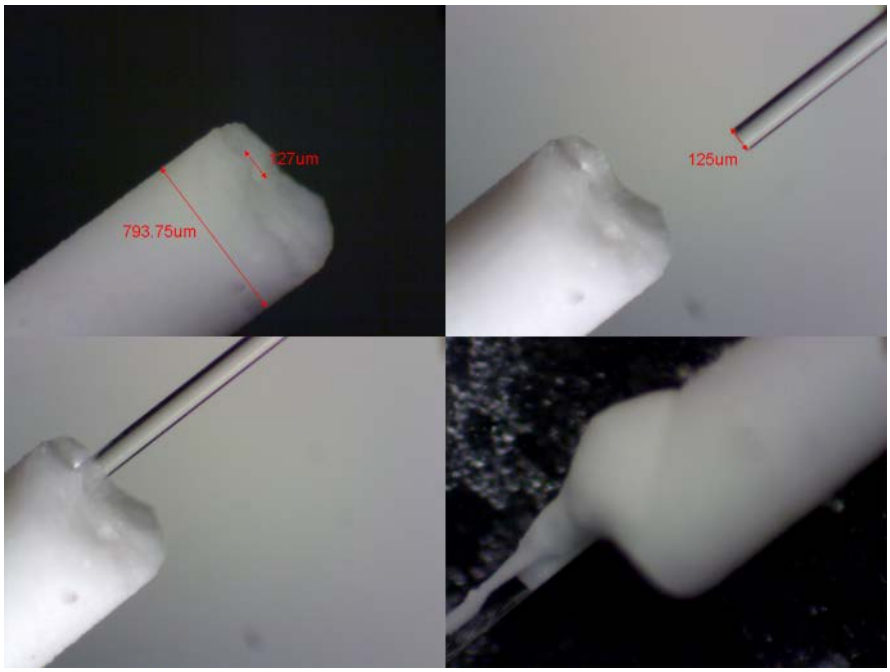

Figure 4-3: optical image of process to guide polished fiber into ceramic tube and bonding

The detailed process is shown in Figure 4-3. After the length of fiber segment inside the ceramic tube reaches the desired value, ceramic glue is used to bond the fiber to the ceramic tube. The whole process is controlled under an optical microscope. The curing of ceramic glue takes about 2 hours at room temperature.

Step 3: Formation of Fabry-Perot cavity

Repeat step one to get another plane surface on the end of the leading fiber. Then repeat step two to guide the fiber end into the ceramic tube. During this process, an interference measurement system is used to in-situ monitor the reflected light. As predicted, when the surface of the leading fiber gets closer to the surface of the fiber segment, the recorded spectrum will shift and also show significant change on fringe density and visibility. The fringe density will decrease, as well as spectrum visibility. Fringe density can be used to roughly calculate cavity length, while accurate initial cavity length is not required. Once the desired cavity length is reached, ceramic glue will be used again to bond the leading fiber to the ceramic tube. The bonding process can cause the cavity length to change due to curing, which means it is hard to preciously control the cavity length at room temperature in this design.

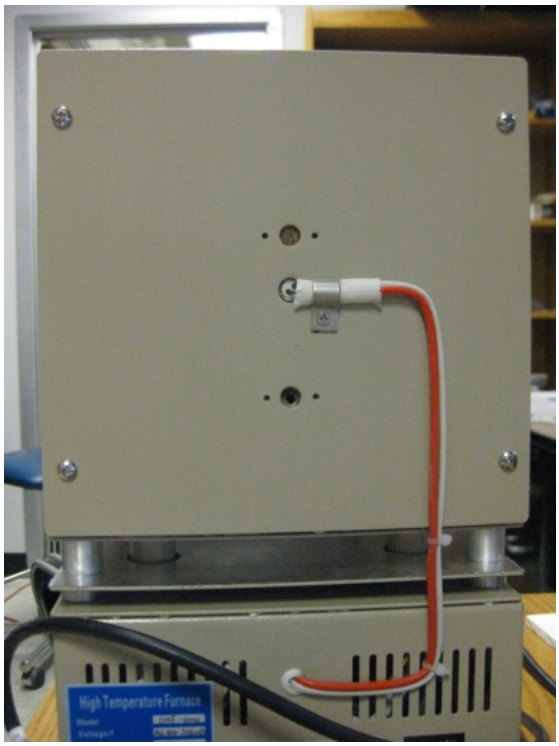

Figure 4-4: furnace we used for anneal

This problem is hard to resolve as long as ceramic glue is used for bonding, because the curing process is hard to control. However, carefully choosing of fringe density before bonding can give different room temperature cavity length.

The sensor fabrication process also includes annealing. The furnace from MTI is used in this process. A hole is drilled on the back panel of the furnace, so we can easily put the sensor into the furnace, shown in Figure 4-4. The annealing process can improve the stability of FPI.

First, the sensor is carefully placed into the furnace through the hole on the back panel, with the leading fiber connected. Then the temperature of furnace is increased from room temperature to 200 ^{o}C, with an increase speed of 10 ^{o}C/min. Then the temperature is kept at 200 ^{o}C for another 2 hours, followed by another temperature increase process with the final temperature as high as 800 ^{o}C. This process takes 1 hour. Then the furnace temperature is kept at 800 ^{o}C for around 24 hours.

4.2 Sensor calibration for temperature application

We used the FPI sensor for temperature sensing application. It needs to be calibrated before use. Since the cavity length is used as the sensitive element in the design, the purpose of the calibration process is to find out the relationship between temperature and cavity length. Furnace and thermal coupler is used for calibration. We placed the thermal coupler and the FPI sensor together into a furnace through the hole on the back panel, making sure that the distance between the thermal coupler and FPI sensor is less than 1 mm so the thermal couple can give out accurate temperature reading for FPI. Then the furnace temperature is programmed to increase and decrease step by step. We recorded the readout of the thermal coupler and corresponding cavity length of FPI sensor

extracted by the data processing techniques as the calibration data. Figure 4-5 shows a calibration curve for one of our FPI temperature sensor, from room temperature to 500 ^{o}C.

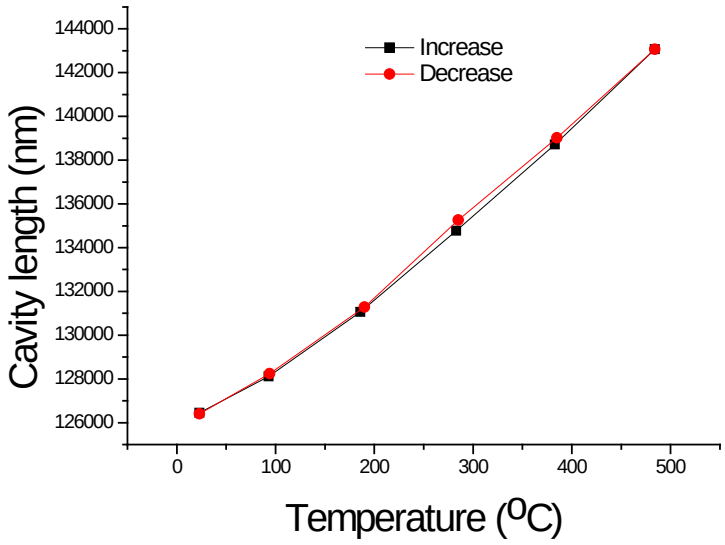

Figure 4-5: calibration curve of sensor from room temperature to 500 ^{o}C

Theoretically, the temperature measurement range is broad for the FPI sensor, depending on whether the material will be permanently damaged or not under certain temperature. The ceramic tube and fiber is stable at temperature as high as 800 ^{o}C, which is good enough for this application.

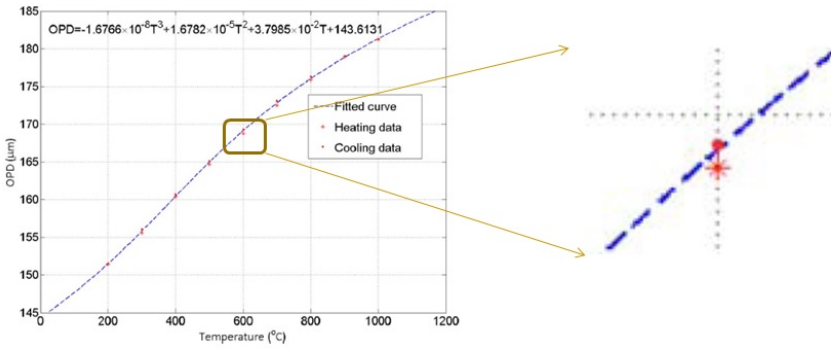

Figure 4-6: Hysteresis problem

In the previous discussion, curve of cavity length as function of temperature, which has an almost linear shape for the temperature range from around 690 ^{o}C to 700 ^{o}C, is

shown. That is because the thermal expansion coefficient of the ceramic tube and fiber does not change much within a small temperature range. For relatively larger measurement range, thermal expansion coefficient of the ceramic tube and fiber will change which can introduce non-linear calibration curve.

The hysteresis problem of the FPI sensor is significant. Figure 4-6 [15] shows the reported hysteresis issue from other group with a similar FPI design. The inaccuracy of cavity length can be as large as around 0.5 μm. We observed a similar hysteresis. From Figure 4-5, it is clear that for heating and cooling process, the cavity length at same temperature is different. The variation of cavity length at same temperature for the temperature increase and decrease process can be around 150 nm or larger in our sensor, which means a temperature uncertainty of about 5 ^{o}C. Such a large temperature variation is not promising for commercialization of the FPI sensor.

To solve this problem, we optimized the fabrication process.

Before any optimization approach is proposed, the reason that causes the hysteresis needs to be addressed. The possible reason is proposed as below: 1) the glass fiber starts to melt at high temperature 2) the ceramic tube crystallizes at high temperature 3) the ceramic glue releases vapor into cavity at high temperature and build up the pressure inside the tube. Several experiments are designed to determine the cause of the hysteresis. First, the fiber segment with shape edge is placed in the furnace and heated to 800 ^{o}C. If fiber will melt, after long time annealing at high temperature the shape of the fiber edge will change. However, a sharp fiber edge is found before and after annealing, which indicates that the fiber melting does nott happen. On the other hand, the maximum temperature given in Figure 4-5 is lower than 500 ^{o}C, which is not high enough for fused

silica to melt. Another possibility is crystallization. If it actually happens, long time annealing should remove this effect. But after long time annealing, the hysteresis still exists. So we believe that the hysteresis is from curing process of the ceramic glue. To verify this conclusion and improve sensor performance, we anneal the ceramic tube bonded with the fiber segment for long time before we guide the leading fiber into ceramic tube and build up cavity. We hope this procedure can remove as much vapor that the ceramic glue gives out at high temperature as possible. This approach causes obvious improvement on sensor performance. The calibration curve for the sensor with optimized fabrication process is given in Figure 4-7. During the temperature increase and decrease process, the difference of cavity length at same temperature is less than 10 nm in most cases, which corresponds to around 0.3 ^{o}C. Right now we cannot conclude that the reason of hysteresis is from the vapor that is given out by ceramic glue at high temperature, but we can conclude that the additional annealing process can actually reduce the hysteresis problem.

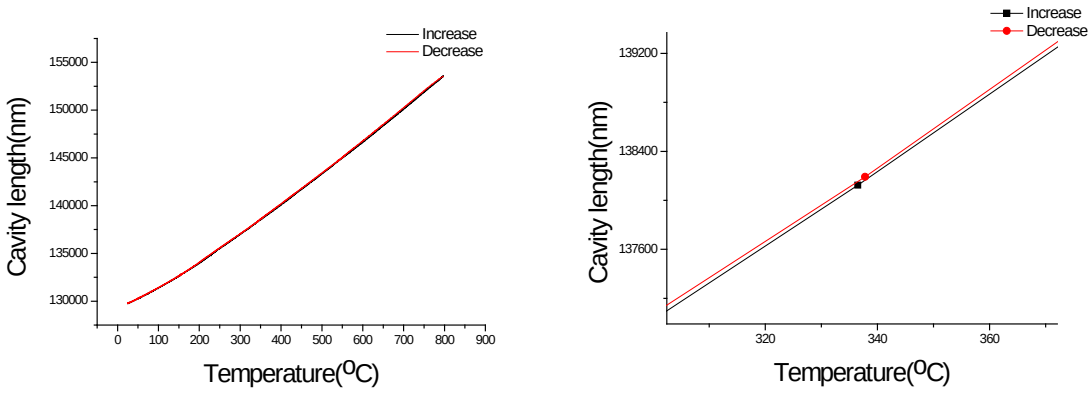

Figure 4-7: optimized calibration curve, with little hysteresis

Chapter 5: Data processing: cavity length extraction

Data processing of the interference spectrum provides the cavity length information. It is a very important part in the development and application of the FPI sensors.

5.1 Introduction

As discussed before, the interference spectrum can be readily described by the following Equation,

$$I = I_0(\lambda) * (1 + A * \cos(\frac{4\pi L}{\lambda} + \pi)), \tag{5.1}$$

where $I_0(\lambda)$ represents the background spectrum. It is directly from the Super Luminescent Diode with wavelength centered at 1310 nm and 90 nm bandwidths. A is parameter related to visibility. L is cavity length and the value that is going to be extracted.

Several approaches can be used to extract cavity length. The most convenient one is the two-peak method, as mentioned before for a rough evaluation of cavity length. In this method, two particular points like peaks or valleys are used for cavity length calculation. In my discussion I use two neighboring peaks, with assumed wavelength λ_1 and λ_2 ($\lambda_1 > \lambda_2$). The interference order of these two peaks is n and $n+1$, respectively. We should have the following Equations,

$$\frac{2 * L}{\lambda_1} = n, \tag{5.2}$$

$$\frac{2 * L}{\lambda_2} = n + 1. \tag{5.3}$$

Here half wavelength loss is ignored without loss of accuracy. From the above discussion, we can easily obtain the cavity length,

$$L = \frac{\lambda_1 * \lambda_2}{2*(\lambda_1 - \lambda_2)}. \quad (5.4)$$

If we can precisely achieve peak position, we can easily obtain cavity length. However in real measurement, it is very hard to obtain peak position with high accuracy. In real measurement we can only achieve accuracy of around 1 μm based on this method, which corresponding to tens of degree difference in temperature measurement.

Another approach that is convenient for application is the peak tracking method. The pre-requirement for this method is that we already know the interference order for one particular peak (valley). By tracking the position of this peak, and using Equation below,

$$\frac{2*L}{\lambda} = n. \quad (5.5)$$

We can achieve relative high accuracy of cavity length information.

Relative error for peak tracking method is low. Temperature resolution based on this method can easily achieve 1 ^{o}C. However, the disadvantage of the peak tracking method is also obvious. First, it has a pre-requirement of interference order information which cannot be obtained by the method itself. So to use this method for real application we have to develop some other technique to accurately extract interference order information. Second, when the data acquisition process is stopped for some reason, the tracking peak is missing.

Our goal is to develop a FPI sensor with high accuracy and long term continuous application. So we focus on development of novel techniques which not only provide high accuracy temperature measurement but also avoid shortage of the peak tracking method. One approach is the fitting method.

We have explained that interference pattern can be described by Equation 5.1. If we can fit this Equation by using cavity length as one of the parameters, fitted cavity length should have high accuracy. Since the spectrum of reflected light is a combination of Gaussian background and interference, it is convenient to do the fitting with normalized data which can effectively reduce the parameters.

5.2 Normalization

Normalization can be divided in to following several steps,

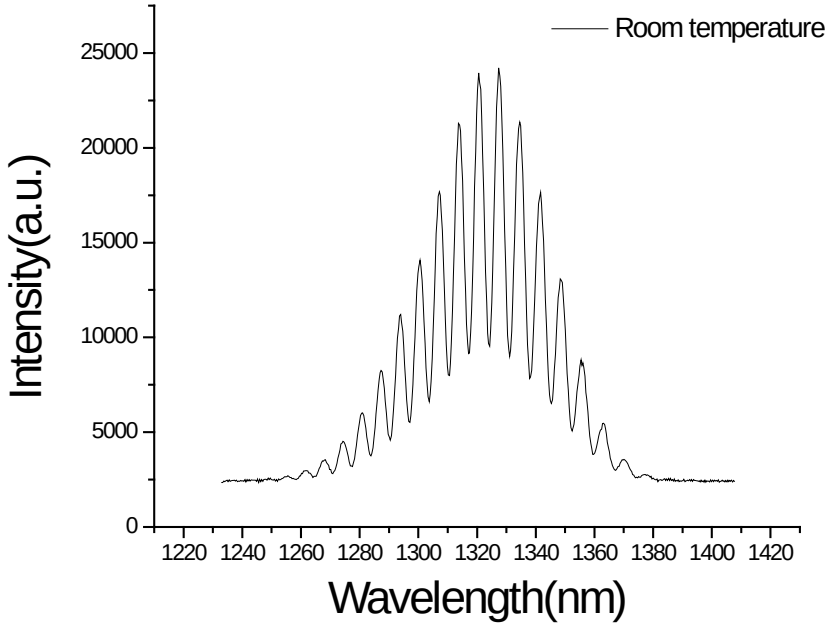

Figure 5-1: Typical interference spectrum

Step1: Baseline removal

The base line removal can be done by simply subtracting the base line value that can either be obtained by dark spectrum measurement, or the intensity read out at the beginning of the spectrum. In our case, we choose the latter approach. Figure 5-1 shows typical interference spectrum.

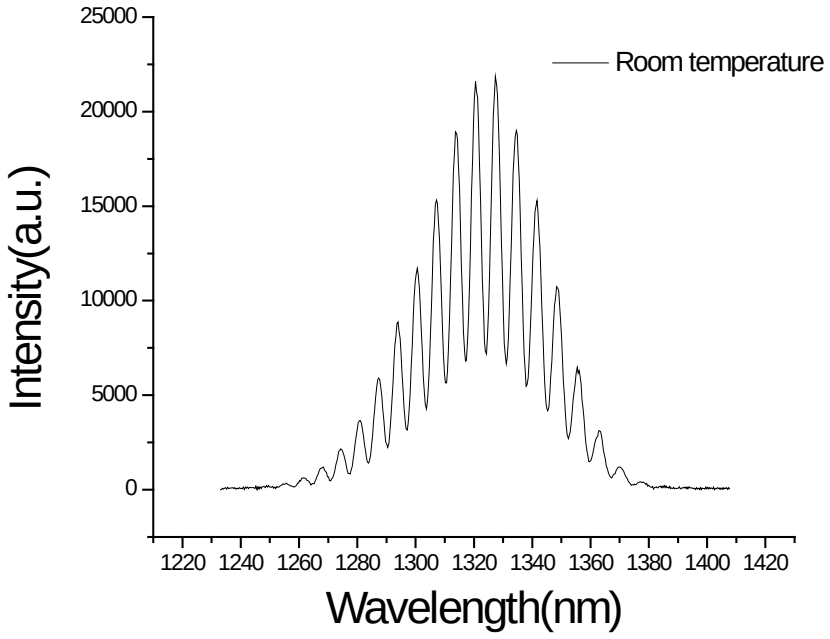

Figure 5-2: Spectrum after baseline removal

Figure 5-2 shows spectrum after removal of base line. The interference pattern will not be affected by this process.

Step 2: Background extraction

After baseline removal, Gaussian background from the light source should be removed for fitting convenience. To do this, we need to first obtain the spectrum of the light source. The straightforward way is to record the spectrum of the light source directly. But results show that with different light source power, the spectrum is different. Peak position shifts and peak width changes. It is not efficient to determine the working power of the light source every time before using FPI. So a method to remove background is necessary. Since Gaussian background has lower frequency compared to the interference spectrum, it is convenient to use FFT low pass filter to obtain the background. The red curve in Fig 5-3 shows extracted background after FFT filter.

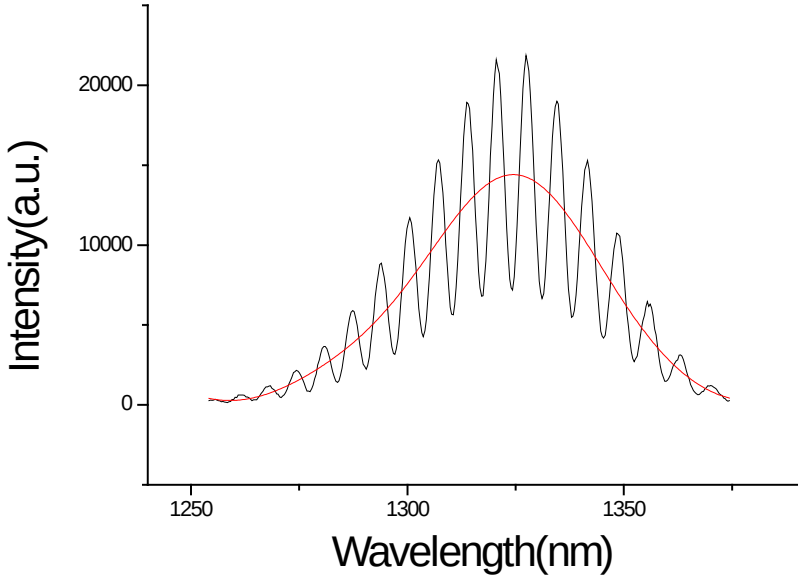

Figure 5-3: Spectrum and background extracted by FFT band filter

Step 3: Remove background

By dividing the original interference spectrum with the extracted background, an interference fringe pattern can be achieved as shown on the left in Figure 5-4. It can be described by Equation 5.1. At the edge of the interference pattern given in Figure 5-4, there are a lot of spikes which are due to the low signal to noise ratio at the tail of Gaussian light source.

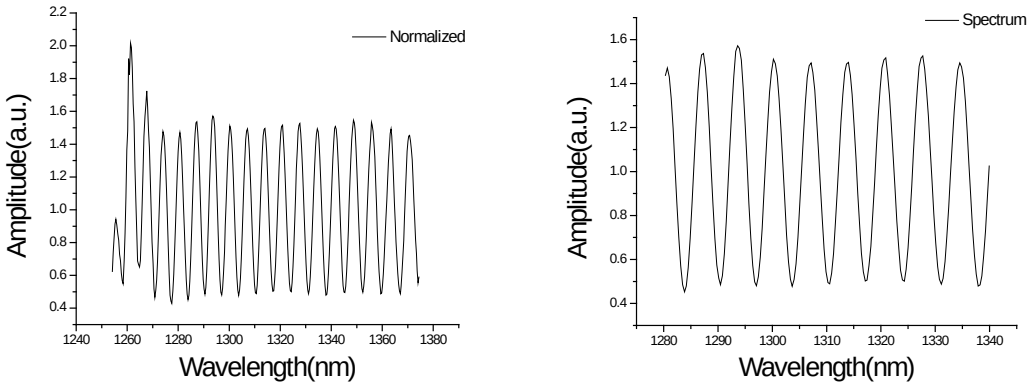

Figure 5-4: Interference spectrum after normalization (left) and spiking removal (right)

These spikes are not good for fitting, so we remove them and only leave interference fringe at center, shown on the right side image in Figure 5-4.

5.3 Fitting approach

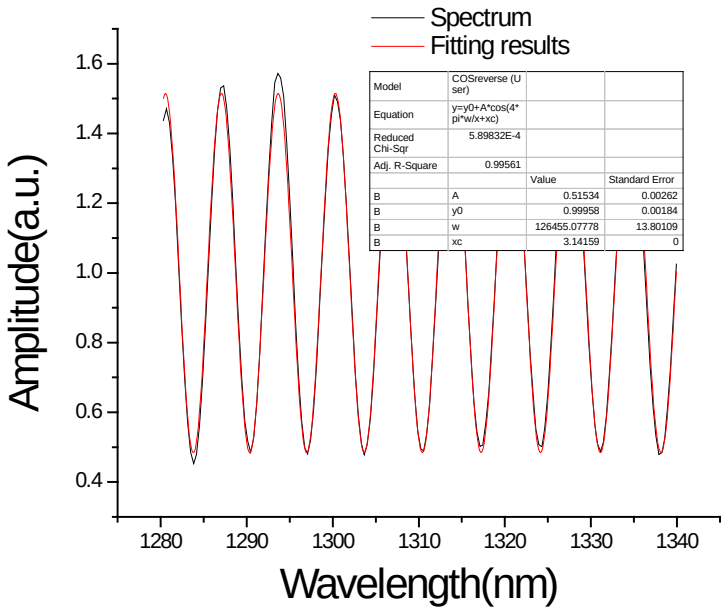

Figure 5-5: Fitting curve and extracted air gap length information

After obtaining the interference pattern without background, we can easily use Equation 5.1 to fit the spectrum. Parameters of the fitting function include amplitude of pattern A, offset K and cavity length L. I use non-linear curve fitting method, which can readily find the best fit by minimizing of reduced chi-square value. Theoretically this method can only guarantee the finding of local minimum but not global minimum. To find global minimum, carefully choosing of initial fitting parameter is critical. Figure 5-5 shows fitting result. A good match is achieved and cavity length is extracted.

Although fitting method is promising in the above example, detailed study and discussion will show that it is difficult to find cavity length by using this method. According to the analysis of the interference spectrum, multiple minimums exist in the

fitting process. It means that if we use different initial cavity length, fitting results will be different. To solve this problem, a straightforward method is to compare the fitting results with full parameter space to obtain the global minimum. Since parameter A and K do not change much in my case, the parameter space is limited to variation of cavity length.

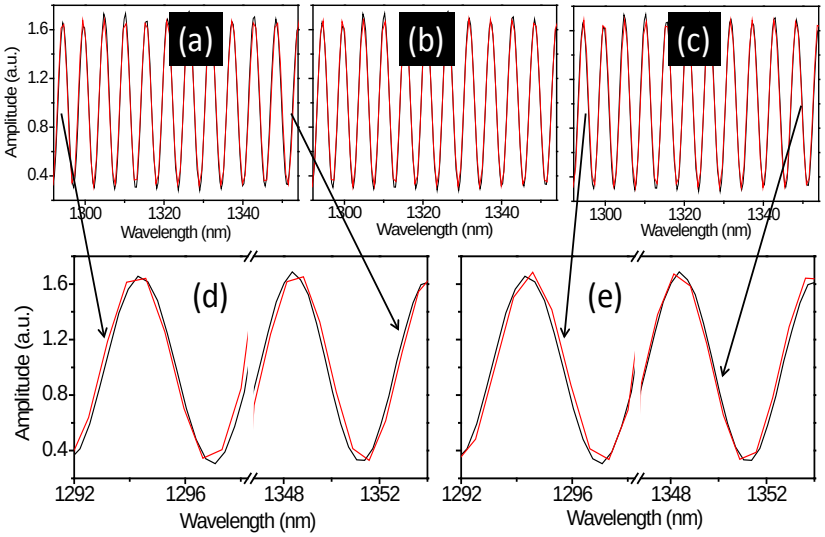

Figure 5-6: Best fit with good initial guess (b) and left shift fit (a) and right shift fit(c). (d) and (e) are zooming in plot

Figure 5-6 shows fluctuation of fitting results. Three neighboring cavity lengths for example will randomly appear as "best fitting" results given by the method during fitting process. Fitting curves from the three lengths are also given. As can be seen, all three fits represent the data quite well, but close-up views reveal that the fits in Figure 5-6(a) and (c) deviate from the original curves at short and long wavelengths. Specifically, the fit in Figure 5-6(d) shows a phase advance near 1294 nm, but a phase delay near 1352 nm. In the central region near 1320 nm, the fit overlaps with the data very well. Based on this observation, we can estimate that the length from this fitting is shorter than the best

fitting cavity length in Figure 6b by λ/2 ~ 660 nm, in agreement with the fitting value. According to the fitting Equation, this difference in cavity length creates a phase shift of 2π near center wavelength of 1320 nm so that the fitting at that wavelength is not affected. The fit in Figure 5-6(e) exhibits an opposite behavior, indicating a longer cavity length by 660 nm. This kind of fluctuation can be resolved sometimes by comparison of reduced chi-square value but not always due to data quality, which means a sudden "jump" or "drop" during automatic data processing.

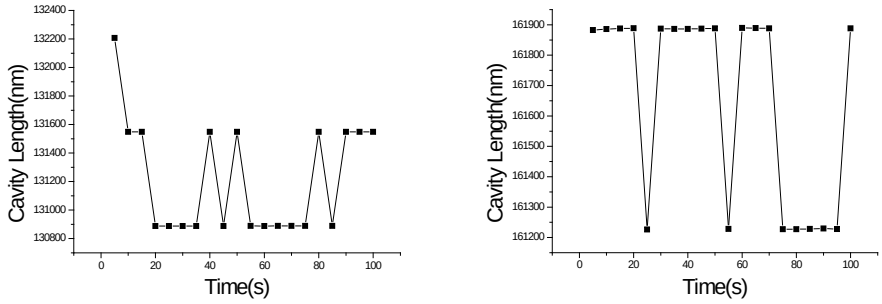

Figure 5-7: fluctuation of fitting cavity length at room temperature and 800 °C

Figure 5-7 shows the fluctuation of fitting cavity length at given temperature. Obvious "jump" and "drop" can be observed. It cannot be resolved by statistical method. This fluctuation is due to data quality and it is the limit of direct fitting method.

5.4 Combination method

In order to resolve the fluctuation problem introduced by the direct fitting method, a special technique is required. Another convenient approach for extracting cavity length is to use wave vector $k = 1/\lambda$ as the new variable. By doing this, the fitting Equation is converted to,

$$I = K + A * \cos(4\pi kL + \pi). \qquad (5.6)$$

It is standard cosine function and has fixed frequency. Now it is easy to directly obtain the frequency of the above Equation by FFT method. It should be noticed that for the initial spectra which is given in Figure 5-4 and 5-5, wavelength λ is used as variable and the data points are almost evenly spaced in λ. The change of variable from wavelength to wave number makes the data point not evenly spaced in wavenumber k. In order to use FFT method to obtain cavity length, we interpolate converted spectrum by using "resampling" method. The cavity length obtained by FFT method as a function of time is given in Figure 5-8, while no obvious "jump" or "drop" is observed.

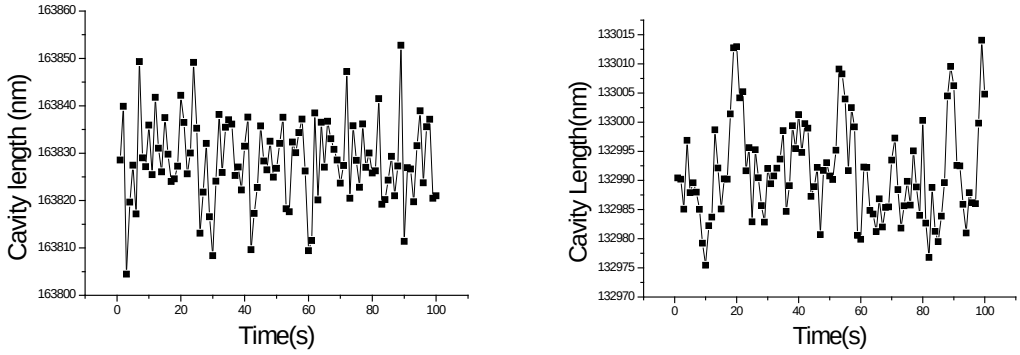

Figure 5-8: cavity length extracted by FFT (room temperature and 800 ^{o}C)

Above discussion demonstrates that FFT technique for cavity length extraction is a convenient and reliable approach, especially for real-time measurement because of fast processing. However, the fluctuation range of cavity length obtained from FFT method is relatively large. Statistical analysis on fluctuation of cavity length obtained by FFT method and peak-tracking method is given in Figure 5-9, which clearly shows that compared to the peak-tracking method, the FFT method provides lower temperature resolution. The standard deviation of cavity length for peak tracking method is 1.49 nm for room temperature, which corresponding to around 0.05 ^{o}C. On the other hand, the

standard deviation of cavity length obtained by FFT method is 13.7 nm, which represents around 0.46 ^{o}C.

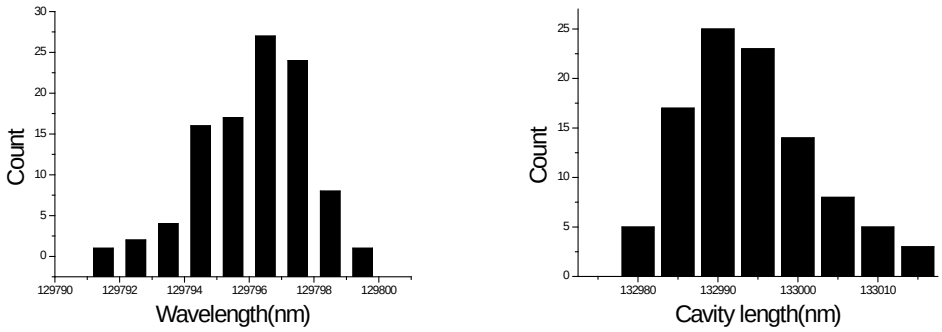

Figure 5-9: statistical analysis on cavity length distribution for peak tracking and FFT method

Fluctuation of cavity length with FFT method is introduced by data quality and determination of frequency during FFT process. The data quality can be improved by careful calibration of spectrometer and better fabrication techniques for FPI. Although 0.46 ^{o}C of temperature fluctuation is acceptable, more accurate temperature measurement is required in some research and application areas and the FPI sensor has capability of higher temperature resolution which is demonstrated by peak-tracking method.

To further improve the temperature resolution of the FPI sensor, a combination of FFT method and fitting method is proposed. As discussed before, FFT method can provide relatively rough cavity length extraction with fluctuation of around 13.7 nm. On the other hand, direct fitting method without good initial fitting parameter is a time consuming technique and has “left shift” or “right shift” problem which is unacceptable. So using the cavity length extracted by FFT method as an initial fitting parameter for the fitting method can solve these problems and provide high accuracy and temperature resolution. Figure 5-10 shows a stable cavity length after using cavity length from FFT to

do the fitting. Fluctuation is reduced to 0.2 nm, corresponding to a temperature resolution of 0.01 °C. As a comparison, we also plot the cavity length obtained using FFT. It should be noticed that room temperature is more stable compared to high temperature in the furnace. We measured cavity length fluctuation for both room temperature and 827 °C in furnace, which is shown in Figure 5-11. Clearly, fluctuation at room temperature is around 0.2 nm, while for 827 °C it can be as high as 1 nm, which corresponds to around 0.05 °C. It is 5 times higher compared with room temperature value. Fluctuation at 827 °C is not completely random. We can observe a cavity length vibration with around 14 seconds period. It should be from the temperature vibration of furnace at 827 °C.

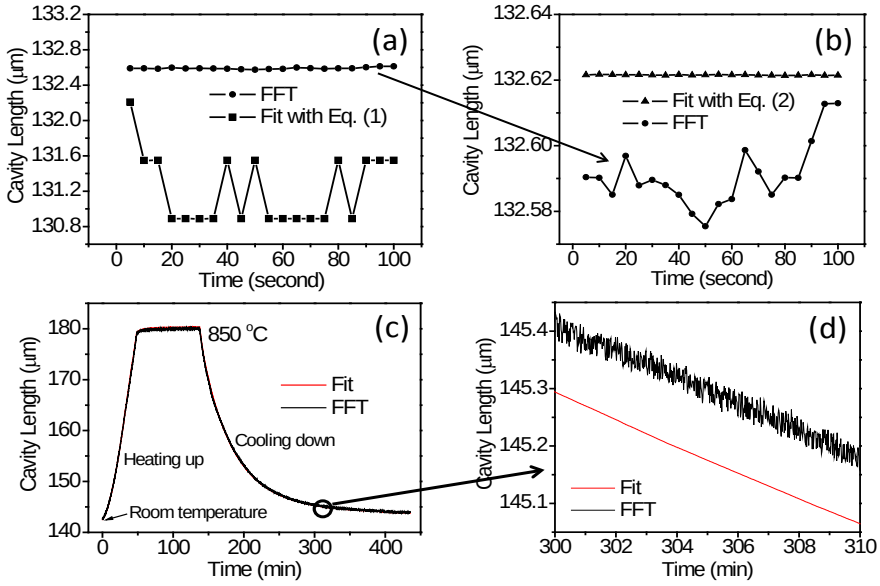

Figure 5-10. Evolution of cavity length calculated using three different methods

As can be seen in Figure 5-10(a) and 5-10(b), the FFT cavity length suffers less fluctuation as compared with the initial curve fitting method which experiences an abrupt "jump" or "drop" problem, but is still as large as 10s nanometers. Note that the FFT cavity length is plotted in both Figure 5-10(a) and 5-10(b), but the scale in Figure 5-10(b)

is 40 times smaller than the scale in Figure 5-10(a). Similar FFT fluctuation was reported before [34].

Figures 5-10(c) and 5-10(d) show the evolution of the cavity length obtained using FFT and the subsequent curve fitting using FFT length as an initial parameter. A clear improvement in temperature resolution can be seen. The length fluctuation from FFT is ~20 nm, corresponding to around one degree. It was also found that results from FFT may not overlap with the result from the curve fitting. This is because the L from FFT is based on the position of the FFT spectrum with the highest intensity, which can be quite different from the position obtained by fitting the FFT peak.

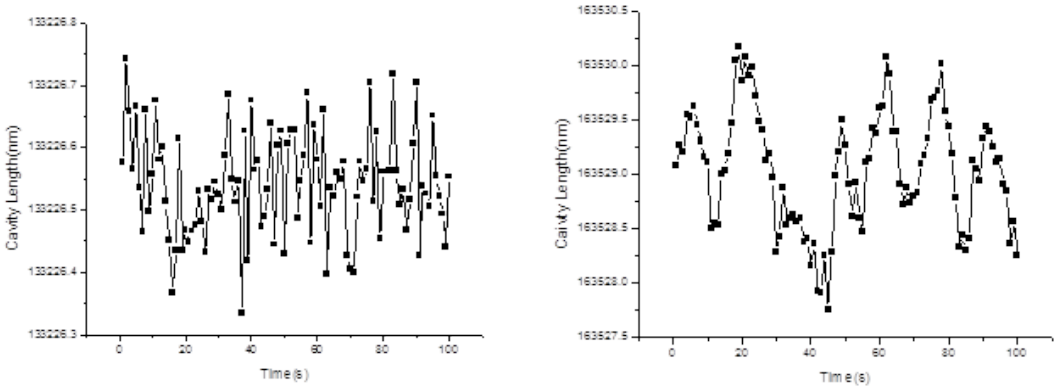

Figure 5-11. Fluctuation of cavity length for combination method at room temperature (left) and 827 ^{o}C (right)

Chapter 6: Visibility simulation

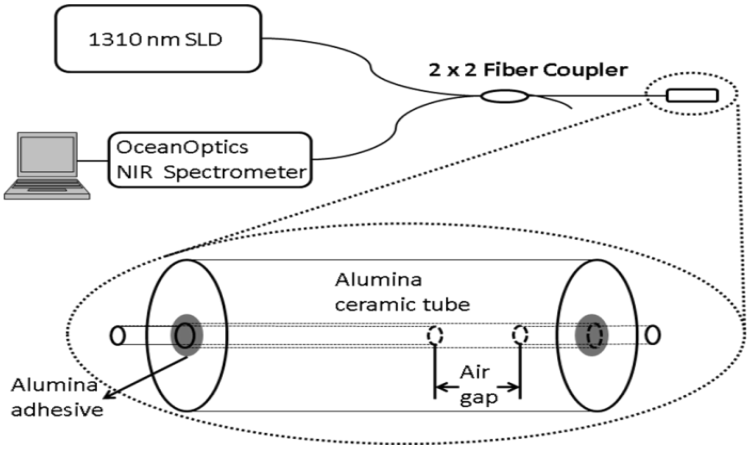

Figure 6-1: schematic illustration of FPI temperature sensor

The basic illustration of a fiber based extrinsic FPI temperature sensor system is given in Figure 6-1. As discussed before, the spectrum visibility is related to cavity length and reflection coefficient.

Consider the light generated by SLD light source on FPI sensor. The light source can be characterized as a Gaussian function [35, 36] as shown in Figure 6-2. The Equation below can be used to simulate background spectrum,

$$y[\mathrm{x}\ \ ] = \mathrm{y0} + \frac{A}{w*\sqrt{\frac{\mathrm{Pi}}{2}}}\mathrm{e}^{\left(-2*((x-\mathrm{xc})/w)^2\right)}, \tag{6.1}$$

where y0 is dark signal generated by spectrometer, xc is center wavelength and w is parameters which can be obtained by analysis of spectrum. For spectrum simulation of Figure 2, $\mathrm{y0} = 364.3$, $\mathrm{xc} = 1310$ and $w = 32.69$. The coherent length of our light source is inversely proportional to the spectral width, and we have,

$$L_c \approx \frac{xc^2}{w}. \tag{6.2}$$

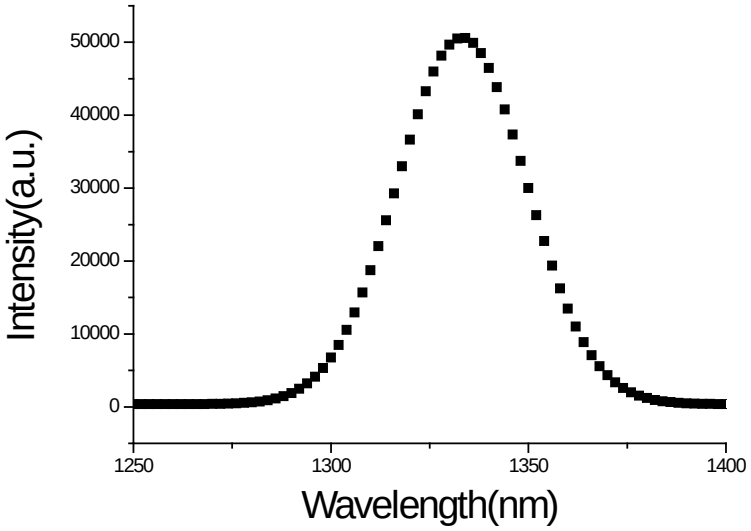

Figure 6-2: Simulated background

The previous discussion indicates that if we assume plane wave propagation the interference intensity at wavelength λ can be described by,

$$I_f = I_0 * [B + (1-B)^2 * D + 2*(1-B)*\sqrt{B*D}*\cos(\frac{4\pi l}{\lambda} + \pi)]. \quad (6.3)$$

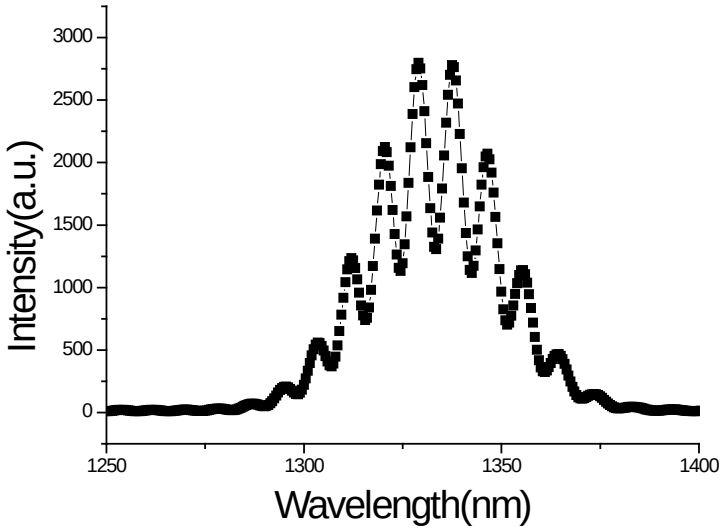

Figure 6-3: Simulated interference spectrum

However, light propagating inside the cavity is not plane wave. The beam size expands when it goes out of the fiber and only part of the light can actually reach the second reflection surface and get reflected, while the other part will be missing. The same process happens when light propagates back and gets coupled into the leading fiber. The portion of missing light is related to cavity length and mode spot size. So if we improve the model and assume we have two surfaces with arbitrary reflection coefficients, the interference can be given by the following Equation,

$$\mathrm{mix[x\ \ ]} = y[x] * \frac{\mathrm{R1}+\eta[L]^2*\mathrm{R2}-2*\eta[L]*\sqrt{\mathrm{R1}*\mathrm{R2}}*\mathrm{Cos}\left[\frac{4*\mathrm{Pi}*\mathrm{n0}*L}{x}\right]}{1+\eta[L]^2*\mathrm{R1}*\mathrm{R2}-2*\eta[L]*\sqrt{\mathrm{R1}*\mathrm{R2}}*\mathrm{Cos}\left[\frac{4*\mathrm{Pi}*\mathrm{n0}*L}{x}\right]}. \tag{6.4}$$

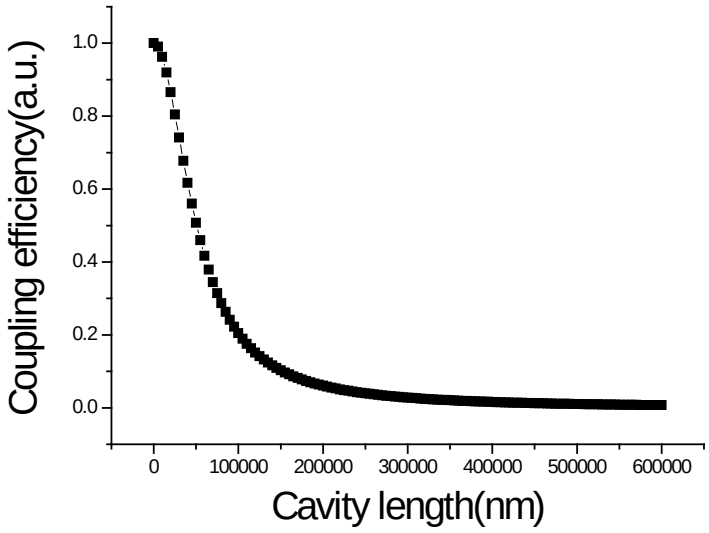

Figure 6-4: Simulated coupling efficiency as function of cavity length

In Figure 6-3, a simulated interference spectrum is given, where cavity length is set to be 100μm and reflection coefficient for first surface and second surface are set to be 0.04 which is the value of silica fiber. η[L_] is the coupling coefficient for the beam travelling inside cavity length, which can be described by the following Equation,

$$\eta[\mathrm{L\_}] = \frac{1}{1+\left(\frac{2*\lambda 0*L}{2*\mathrm{Pi}*\mathrm{n0}*\omega^2}\right)^2}. \tag{6.5}$$

The coupling coefficient is related to cavity length and fiber mode spot size. In our case the fiber mode spot size is 4600 nm.

Clearly the coupling coefficient decreases quickly when the cavity length increases, which is due to relatively small mode spot size. The fast decrease of coupling coefficient causes visibility of spectrum decreases for the above model. The fringe visibility, as defined in the previous chapter, can be given in the following Equation,

$$\text{visi}[L\ ] = \frac{I_{man} - I_{min}}{I_{man} + I_{min}}$$

$$= \frac{\left(\frac{R1+\eta[L]^2*R2+2*\eta[L]*\sqrt{R1*R2}}{1+\eta[L]^2*R1*R2+2*\eta[L]*\sqrt{R1*R2}} - \frac{R1+\eta[L]^2*R2-2*\eta[L]*\sqrt{R1*R2}}{1+\eta[L]^2*R1*R2-2*\eta[L]*\sqrt{R1*R2}}\right)}{\left(\frac{R1+\eta[L]^2*R2+2*\eta[L]*\sqrt{R1*R2}}{1+\eta[L]^2*R1*R2+2*\eta[L]*\sqrt{R1*R2}} + \frac{R1+\eta[L]^2*R2-2*\eta[L]*\sqrt{R1*R2}}{1+\eta[L]^2*R1*R2-2*\eta[L]*\sqrt{R1*R2}}\right)}, \quad (6.6)$$

and with R1=R2=0.04, the visibility simulation is shown in Figure 6-5.

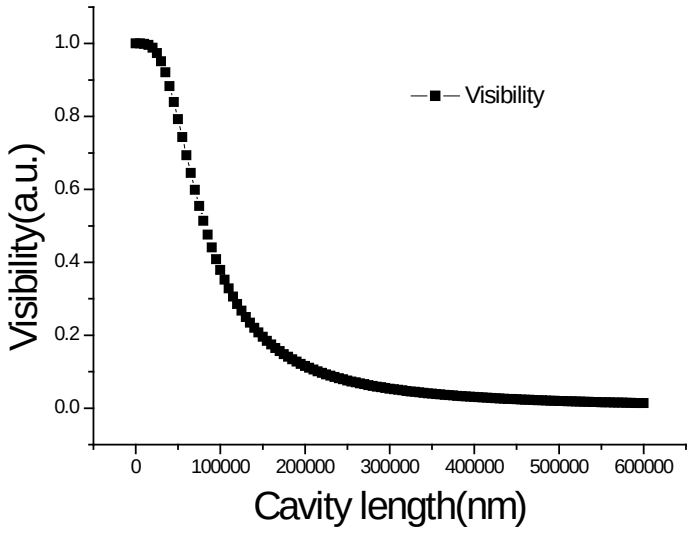

Figure 6-5: Simulated visibility as function of cavity length, with R1=R2=0.04

High visibility means high spectrum quality. Sensor visibility is affected by cavity length, reflection coefficient of fiber and also coupling coefficient which is related to mode spot size. Mode spot size of fiber is determined when fiber is chosen (in our case

we use SMF-28E commercial single mode fiber with mode spot size around 4600 nm). To simulate the visibility as function of cavity length, we can modify the surface reflection coefficient of the leading fiber and fiber segment. The curve shown in Figure 6-6 represents visibility simulation with different R_1 and R_2. It is obvious that as the reflection coefficient of the second surface increases, the visibility peak position shifts to the right side. So to obtain high visibility in our measurement range which is around 50-150 μm, the reflection coefficient of the second surface should be around 0.5 and 10 times larger than the reflection coefficient of first surface.

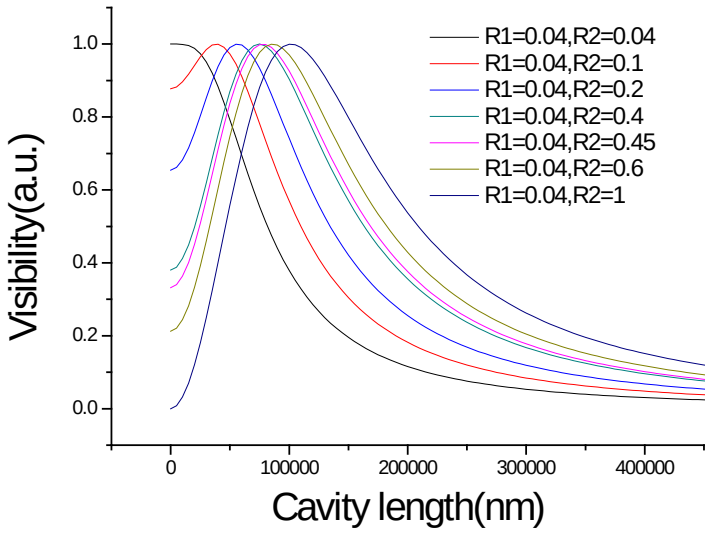

Figure 6-6: Simulated visibility as function of cavity length, with various R1 and R2

The increase of cavity length will cause the fringe density to increase. Here we present that the increase of cavity length will also cause the fringe visibility to decrease for FPI with same reflection coefficient cavity.

Chapter 7: Visibility improvement

7.1 Address visibility controversial to obtain better quality control

According to the discussion in previous chapter, visibility of low-finesse FPI sensor decreases very quickly as given in Figure 7-1.

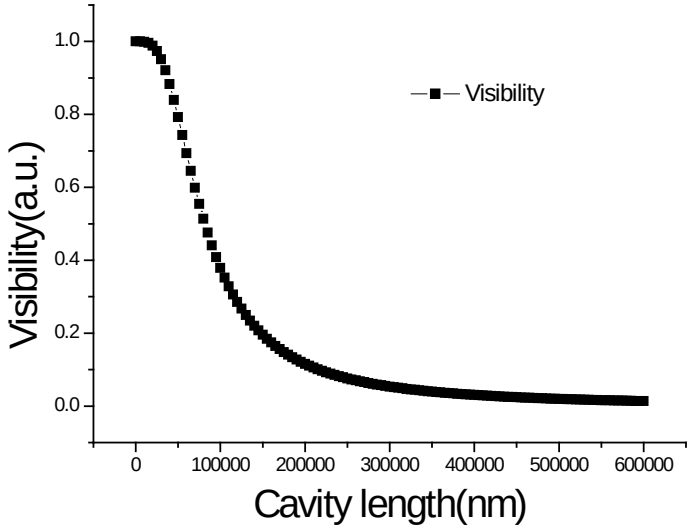

Figure 7-1: visibility simulation for FPI sensor

The visibility curve as function of cavity length is greatly affected by the sensor design. Even for similar design the curve might be different due to material selection. In our design we use single mode fiber (SMF-28e) with mode spot size of about 4600 nm. The theoretical reflection coefficient of single mode fiber we used is about 0.04. Simulation curve given in Figure 7-1 is based on the above parameters. Visibility does not change much when cavity length is smaller than 25 um, but exhibit fast decrease when cavity length becomes larger. In our experiment setup, cavity length is difficult to extract when it is smaller than 25 μm due to data processing limit. But we can compare the trend of visibility with larger cavity length. Also, we can modify the effective

reflection coefficient of fiber by changing the surface preparation method, which can cause the visibility peak to shift to larger cavity length for comparison.

For above design with perfect fiber end, visibility of the spectrum should decrease to less than 0.4 when cavity length is larger than 100 μm according to simulation. But in our experiment, visibility of 0.6 is obtained when cavity length is larger than 100 μm, shown in Figure 3-9. As high visibility represents high quality of sensor, it is important to find out the reason for abnormally high visibility so we can further control the quality of FPI. According to the theoretically analysis, visibility is mostly affected by coupling efficiency of Fabry-Perot cavity which is related to mode spot size of fiber and effective reflection coefficient of two parallel surfaces. We use commercial single mode fiber (SMF-28e). It can provide high visibility compared with other single mode fiber [37]. Another parameter that can affect the visibility is the effective reflection coefficient. The reflection coefficient of silica fiber is around 0.04. But in reality the effective reflection coefficient is affected by surface condition. Since our results indicate abnormally high visibility compared to simulation results, and mode spot size of fiber is not the reason based on the above discussion, we believe that high visibility of our sensor should be from the different effective reflection coefficients of two fiber surfaces introduced by surface preparation techniques. To confirm this hypothesis several experiments are designed. A fiber segment with the highest effective reflection coefficient is used, along with a ceramic tube to build up the second reflection surface, while the effective reflection coefficient of the leading fiber is adjusted and visibility trend is observed.

7.2 Experiment design

For each experiment, we use a 3D stage to control the cavity length and obtain the interference spectrum. The experimental design is similar to the fabrication process of FPI sensors that we already discussed before, except that we do not use ceramic glue to bond the leading fiber to the ceramic tube so we can easily adjust the cavity length. Figure 7-2 shows the schematic drawing of experiment design for visibility measurement. Since fiber diameter is 125 μm and pore size of ceramic tube is 127 μm, fiber is confined inside the pore with good alignment on the direction of tube. This setup enables that two surfaces are placed parallel to each other when fiber surface is perfectly perpendicular to the axis of fiber. By data processing with the obtained interference spectrum, we can obtain cavity length and visibility information. Visibility as function of cavity length is plotted based on the above approach. For the purpose of comparison, simulation with different effective reflection coefficients is also done. Although the accuracy of cavity length obtained by these methods is limited when cavity length is too small or too large, it is acceptable in visibility discussion.

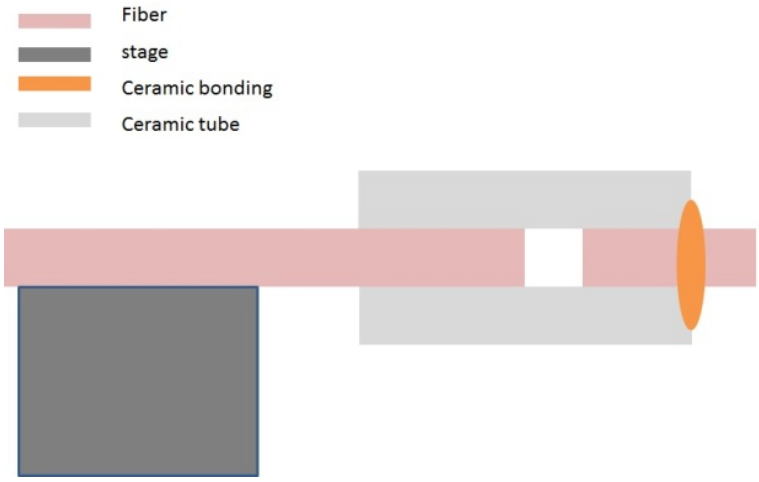

Figure 7-2: schematic drawing of set up for visibility experiments

7.3 Results and discussions

To compare visibility obtained by the above method with simulation results, it is necessary to first obtain the effective reflection coefficients of the two surfaces before building up the cavity. The effective reflection coefficient is not ideal value of silica fiber. It is easy to get this value by measuring the spectrum of reflected light directly from the light source. This can be done by using a fiber coupler with 50/50 coupling efficiency. For effective reflection coefficient calculation, coupling efficiency of the fiber coupler needs to be considered. It is convenient to do measurement on the leading fiber, while for the fiber segment what we have done is to measure the effective reflection coefficient before cutting it from the fiber coupler and bonding it with ceramic tube. The bonding process won't affect the fiber surface which has been confirmed. To calculate the effective reflection coefficient, the spectrum from the light source is also needed. Figure 7-3 shows the spectrum of reflected light that we recorded from the leading fiber, fiber segment and spectrum directly from the light source for the first experiment. It should be noticed that the spectrum from the light source is saturated so we decrease the integration time. The spectrum recorded from light source represents the light that has gone through fiber coupler so coupling efficiency is 50%, while reflection spectrum has gone through the fiber coupler twice and has 25% of coupling efficiency.

Based on the above discussion, we calculate the effective reflection coefficient. For the first experiment set, a similar effective reflection coefficient for the two reflection surfaces is desired. It is difficult to obtain completely the same effective reflection coefficient, but from the calculation we can obtain the effective reflection coefficient of around 0.017 for lead in fiber and 0.0181 for fiber segment, which is quite close. The

power of the light source we used is 0.5 mw, with Gaussian shape peaked at around 1350 nm.

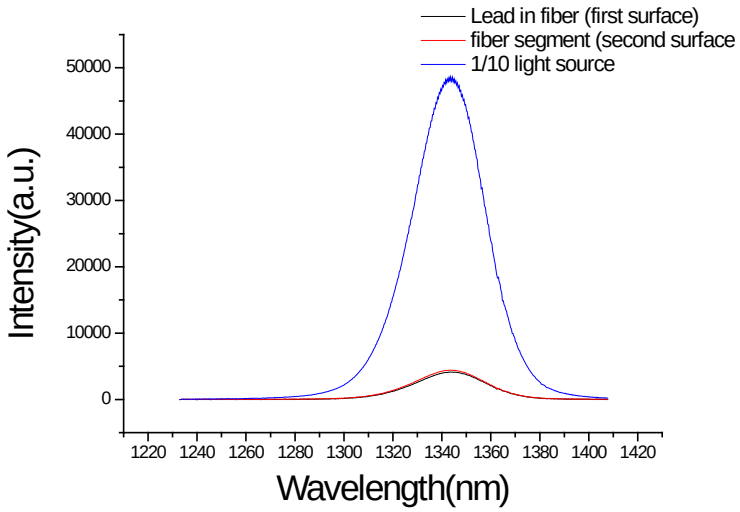

Figure 7-3: spectrum recorded for reflection light and light source

Then we obtain the interference spectrum by carefully moving the leading fiber with a 3D stage. Using data processing techniques that we discussed before, cavity length is easily calculated. The visibility can also be calculated by definition. For the simulation part, the parameter is 4600 nm for mode spot size, 0.017 for effective reflection coefficient of lead in fiber and 0.0181 for fiber segment. Figure 7-4 shows visibility as function of cavity length for experimental and simulation results. The two curves both show a decrease of visibility when cavity length increases while the slope of the simulation curve is larger than experimental data when cavity length is less than 200 μm. Also it should be noticed that for this experiment, visibility decreases to around 0.4 or less when cavity length is larger than 100 μm for both simulation and experiment result.

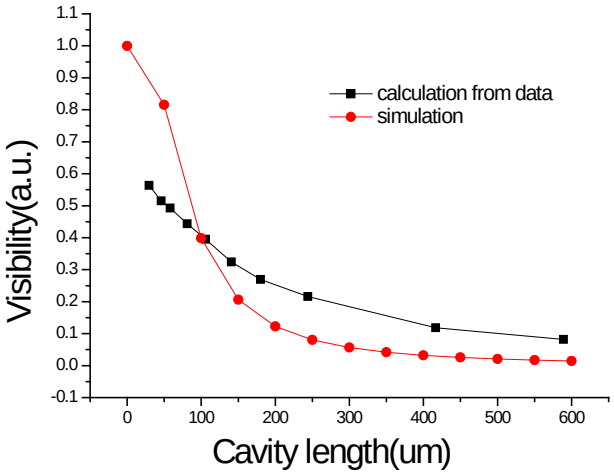

Figure 7-4: visibility calculated from data and simulation comparison

Simulation of visibility predicts that peak position of visibility will shift to larger cavity length when the effective reflection coefficient of the leading fiber is smaller than that of the fiber segment. By using different surface preparation techniques for the leading fiber we can obtain different effective reflection coefficients. Figure 7-5 shows the relative Gaussian spectrum of light from the modified leading fiber, fiber segment and light source.

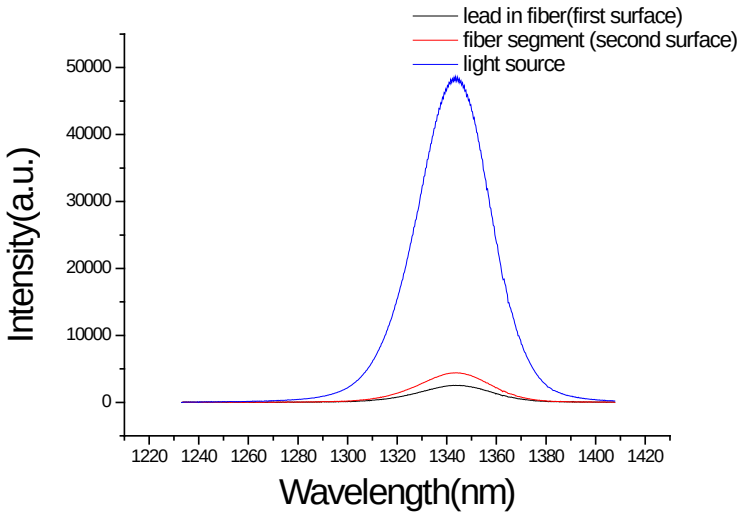

Figure 7-5: spectrum recorded for reflection light and light source

The spectrum from the fiber segment and light source is kept at same value, while the effective reflection coefficient of the leading fiber decreases to about half of its original value. By calculation, an effective reflection coefficient of 0.01 is obtained for the leading fiber. According to simulation, peak position of visibility in this setup is smaller than the cavity length range that can be extracted by data processing. So what we can expect from experimental data is still a decrease of visibility when cavity length increases which is shown in Figure 7-6.

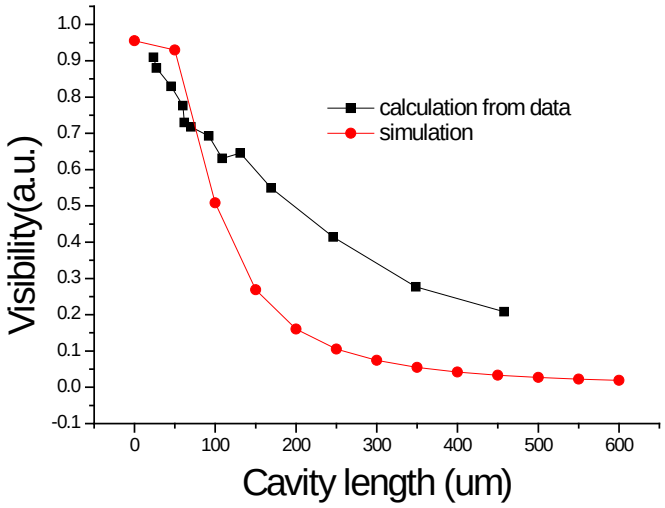

Figure 7-6: visibility calculated from data and simulation comparison

The difference between the above two experiments is that visibility of the second experiment should be larger than the first experiment at same cavity length based on simulation results, which is observed and plotted in Figure 7-7. Clearly at the same cavity length, interference spectrum with smaller effective reflection coefficient of the leading fiber gives higher visibility. At around 100 μm cavity length, the visibility for this setup can be as high as 0.65, while for another setup the visibility is less than 0.4.

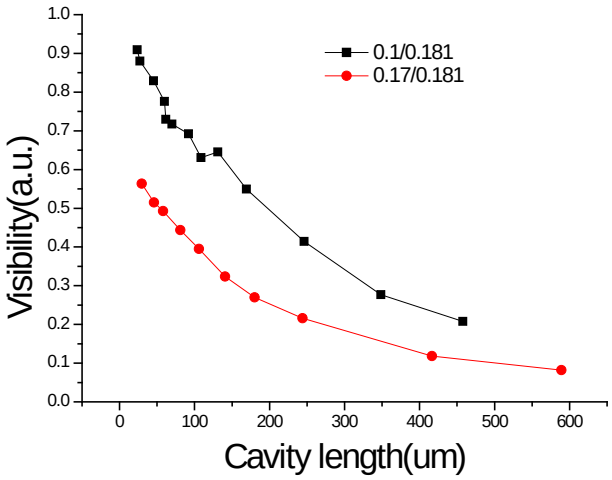

Figure 7-7: comparison of visibility calculated from data

The comparison of two experimental results has already supported the hypothesis that high visibility could be achieved with different effective reflection coefficient. But the shift of visibility peak is strong evidence for this conclusion. So we further reduce the effective reflection coefficient of the leading fiber and do a similar experiment. The reflected spectrum from light source and fiber is given in Figure 7-8.

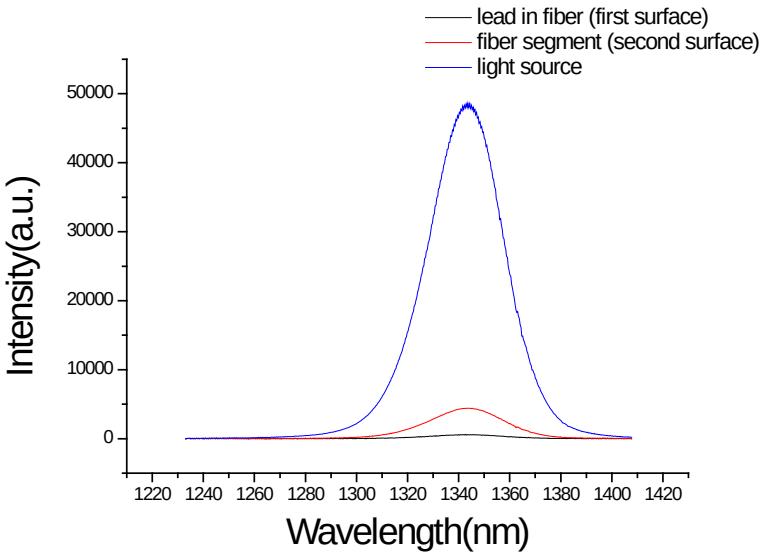

Figure 7-8: spectrum recorded for reflection light and light source

At this time, the effective reflection coefficient is reduced to 0.0022 for the leading fiber, which is almost ¼ of the value compared with the second experiment. The calculated visibility and simulation results are given in Figure 7-9.

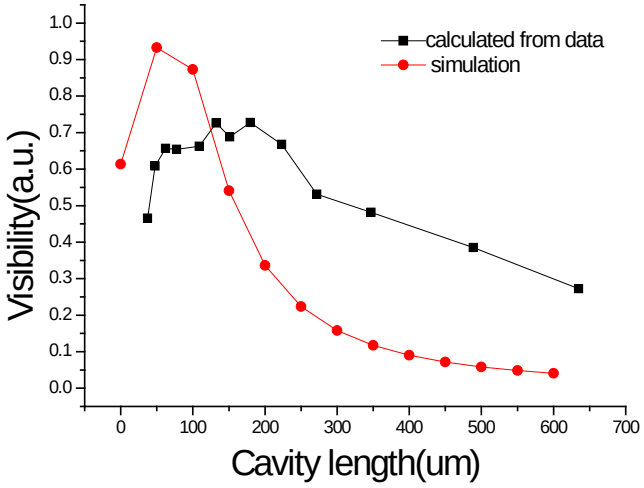

Figure 7-9: visibility calculated from data and simulation comparison

The maximum visibility for experimental results is located at cavity length around 100 μm. The data point is not perfect due to spectrum quality, but it does prove that peak position of visibility shifts to a larger cavity length when decreasing the effective reflection coefficient of first surface. The peak position for simulation result and experimental result is close and has similar intensity.

It should be noticed that above experimental results with different effective reflection coefficients for the first reflection surface do not perfectly match with simulation results. The reason for this observation should be attributed to the alignment of the two fiber surfaces. For FPI sensor, the cavity surface should be perfectly perpendicular to the axis of the fiber, but in real fabrication process it is impossible. There will always be misalignment for the two surfaces and the misalignment angle could change when cavity length is adjusted.

Chapter 8: Phase problem

8.1 Introduction

In previous discussion, an Equation below is used to describe the interference pattern,

$$I_f = I_0^{'} * (1 + A\cos(\frac{4\pi L}{\lambda} + \pi)). \quad (8.1)$$

This is based on plane wave interference theory.

However, light traveling outside the fiber cannot always be considered as plane wave, so interference theory discussed before needs to be modified. The purpose of study on additional phase is to accurately extract cavity length. Different models have been proposed to theoretically predict the additional phase. One model attributes it to free space beam propagation when light is inside cavity and coupling of reflected light at the leading fiber surface [37].

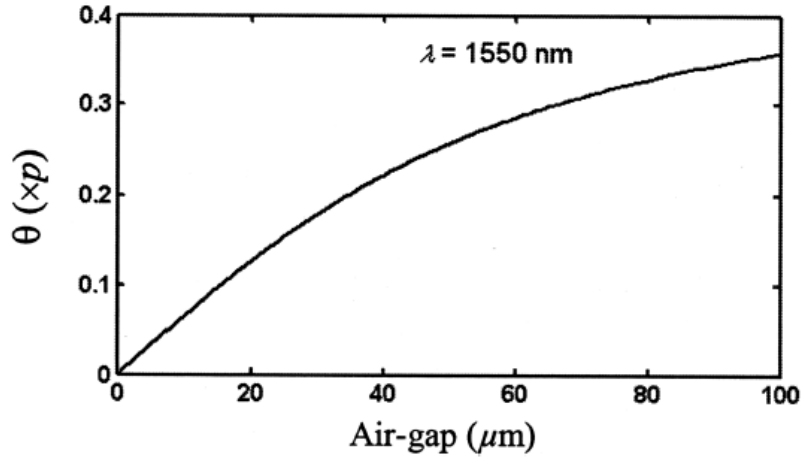

Figure 8-1: Simulation on additional phase term

Additional phase as function of the cavity length predicted by this coupling model is shown in Figure 8-1[37]. For incidental light with 1550 nm wavelength, the additional

phase ranges from 0 to around 0.35 when cavity length increases from 0 to 100 μm. The range of additional phase is quite limited depending on the parameters.

Another model calculates plane wave propagation of light inside the fiber cavity with different z direction wave-vector component which experiences different OPD [38].

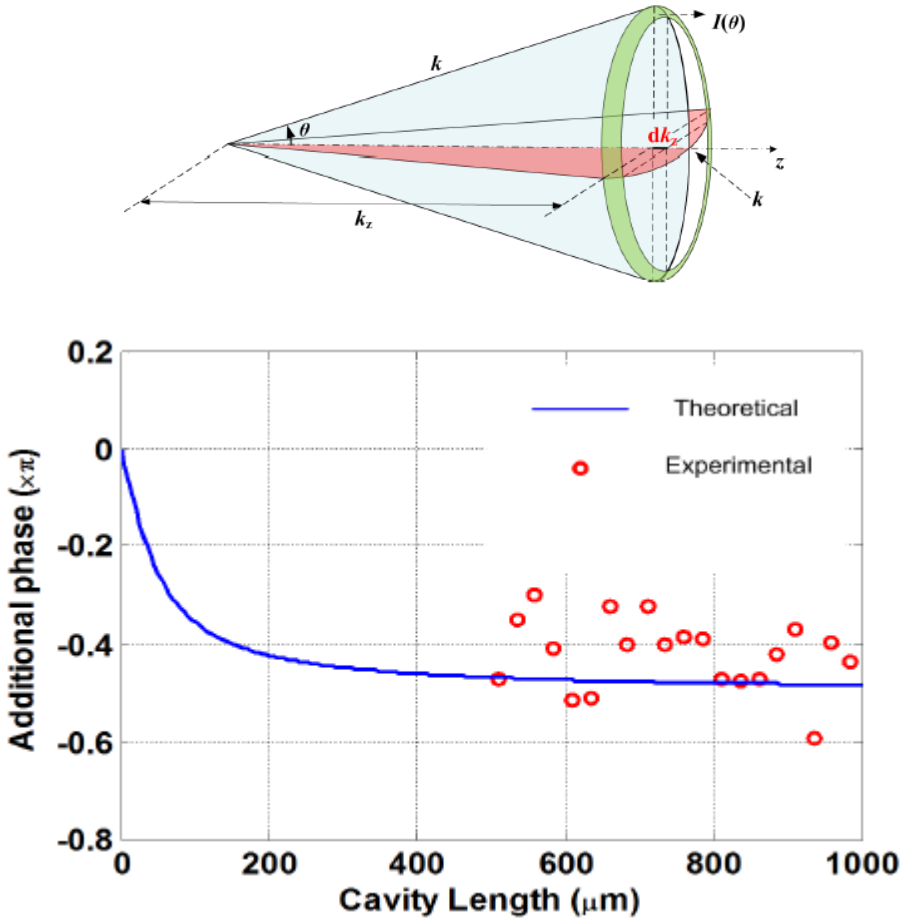

Figure 8-2: Schematic drawing to show beam expansion when light travel outside fiber (top) and simulation and experimental data for additional phase (bottom)

This model, in principle, is similar to the explanation of coupling model [37]. The top image in Figure 8-2[38] shows the beam expansion when light travels outside the fiber into the cavity. The coupling model actually treats the difference between average OPD of the beam inside the cavity and the calculated OPD by perpendicular light as the

effective additional phase, while in the above model a propagation wave vector is used instead. As can be seen, two models actually give a similar prediction of additional phase which is shown as the blue curve on the bottom image of Figure 8-2.

Although simulation of additional phase has been reported, experimental data of it at small cavity length that can be used for comparison and confirmation is still lacking due to data processing difficulty. As shown in the bottom image of Figure 8-2, the additional phase for cavity length smaller than 450 μm is missing due to data processing difficulties. That is because the additional phase is a function of both wavelength and cavity length and is usually coupled into effective cavity length, while high density interference fringe is necessary for additional phase extraction through the method given in [38].

8.2 Novel technique for additional phase extraction

In this dissertation, a novel technique is proposed for the additional phase extraction.

From theoretical prediction, the additional phase φ is related to the cavity length and wavelength of incidental light which means for a fixed cavity length there is a phase distribution in wavelength space. But in a small wavelength range, the additional phase distribution is relative stable. In our FPI measurement system, the spectrum range is from 1280 nm to 1360 nm which is relatively narrow. It is reasonable to treat the additional phase distribution to be constant so it is sole function of the cavity length.

Now let us consider the data processing techniques that have been discussed for the cavity length extraction. From theoretical prediction, we can reach the conclusion that the peak tracking method will give cavity length with an additional phase coupled inside. The peak tracking method is based on the Equation below,

$$\frac{2L}{\lambda} = n, \tag{8.2}$$

where L is cavity length, λ is wavelength of selected point (usually peak or valley of spectrum), n is interference order.

Since the additional phase is introduced by the fact that light coupled back into the leading fiber usually has a slightly different OPD because of the free space propagation. The cavity length L in above Equation actually represents the "average" OPD of multiple beams inside cavity. So the extraction of cavity length by the peak tracking method actually provides the coupled OPD which includes both the absolute cavity length and additional phase. So this method cannot be used to extract absolute cavity length.

On the other hand, the direct fitting method might be used for absolute cavity length extraction, only under the condition that we already know the additional phase before fitting. That is because a perfect fitting can only be reached with perfect data quality, in which the effect of additional phase is not distinguishable. To confirm this conclusion, we record the interference spectrum at the same cavity length and use fitting method with the additional phase as fitting parameter to extract cavity length. The fluctuation of cavity length and additional phase are large random in an unpredictable manner. Also to confirm the coupling effect of the cavity length and additional phase, we do the fitting with a constant additional phase changing from -0.5 to 0.5. Figure 8-3 shows the plot of extracted cavity length as a function of the additional phase which is set to be constant in the fitting process. An obvious correlation between the two values is be found, which means originally the additional phase is required before fitting if absolute cavity length extraction is necessary. Although the phase-coupled cavity length that can be extracted by fitting with additional phase equal to π is good for temperature measurement, the

accurate extraction of the additional phase is still required for some situation and obviously the direct fitting method cannot provide this information.

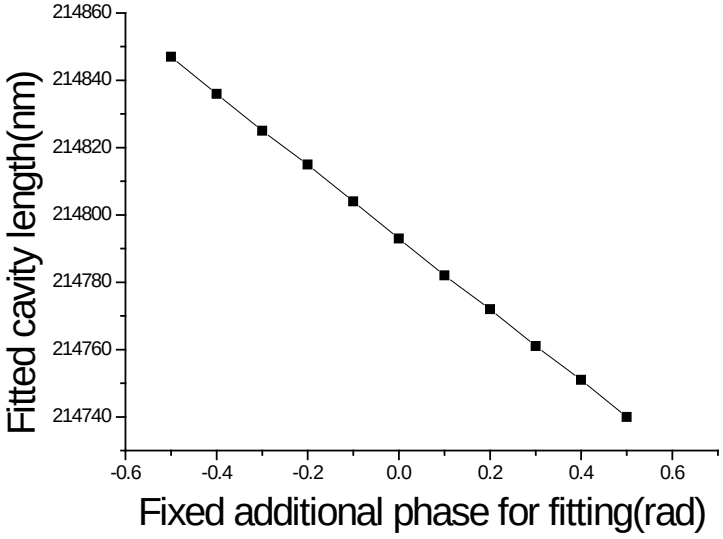

Figure 8-3: Correlation between additional constant phase for fitting and fitted cavity length

Now we focus on the FFT method for cavity length extraction. Based on the FFT theory, by tracking of FFT peak in momentum space, the cavity length can be obtained because it is directly related to the frequency of the interference spectrum after the variable is changed from wavelength to the wave vector. The reason why FFT is not a good method for absolute cavity length extraction is due to its low resolution compared with the peak tracking method and the fitting method. According to our previous results, the fluctuation of FFT method can be 10s nm, which corresponds to around 0.5 ^{o}C in temperature measurement. But on the other hand, the cavity length that obtained by the FFT method is not phase coupled because of its working mechanism. The FFT method directly obtains the frequency information from the interference spectrum which is determined solely by cavity length. So by using FFT method, we can obtain absolute cavity length.

Based on the above discussion, we proposed to combine the FFT method and direct fitting method to extract the additional phase. The FFT method is used to obtain absolute cavity length, while the fitting method is used to obtain phase coupled cavity length with a much smaller fluctuation compared with the FFT method. The difference of cavity length between the values obtained by above two methods should represent the additional phase, based on the above analysis. The additional phase obtained by this method has a fluctuation which is determined by the FFT fluctuation. 10 nm fluctuation of cavity length is corresponding to around $0.03\ \pi$, which is the resolution of additional phase that can be obtained by this method.

Figure 8-4 shows the plot of additional phase that is obtained by using above method as function of cavity length. It should be mentioned that smoothing has been applied on the curve. There is a systematic and continuous difference between cavity length obtained by the FFT method and fitting method, which indicates the existence of additional phase. Also the plot in Figure 8-4 includes both the cavity length increase and decrease process, while two processes give a similar additional phase trend although the peak position shows slightly shift.

The additional phase observed does not perfectly match with the theoretical prediction by other groups. Based on the above discussion, we believe that in principle the combination method for additional phase extraction is feasible. The mismatch between the calculated additional phase and theoretically predicted value either indicates that the modification of theoretical model is required, or other mechanism could exist for contribution of additional phase like alignment of the cavity and surface condition. Further work on additional phase will be done based on this method.

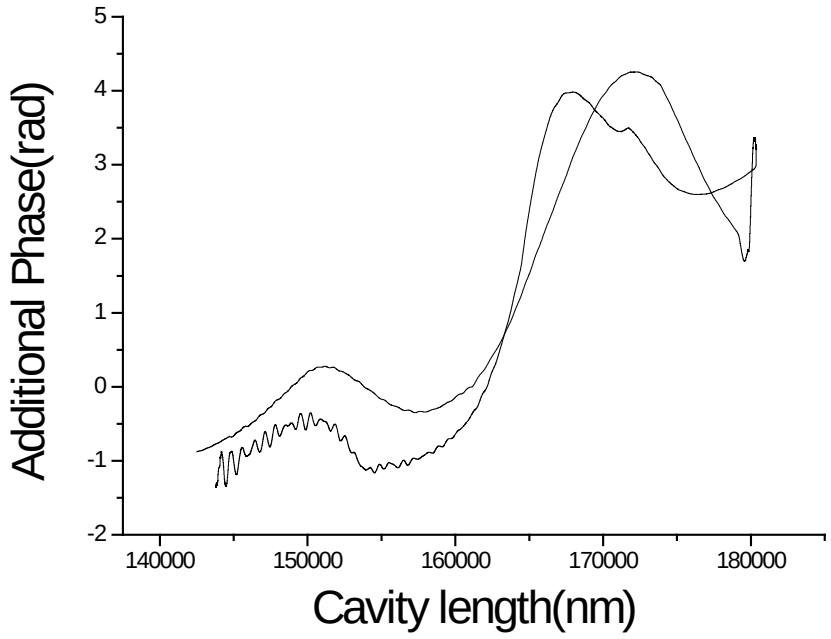

Figure 8-4: Additional phase term extracted by combination method

Chapter 9: Sensor calibration, stability, specification and multiple sensor system

9.1 Sensor calibration

FPI sensor is used for temperature detection. The detection process includes data acquisition and processing. The data acquisition can be done by a computer controlled spectrometer so the recorded data can readily be used for the data processing. Techniques that have been discussed in previous chapter can be used to accurately extract cavity length. To find temperature information, the calibration of sensor which gives relationship between temperature and cavity length is required. Since it is difficult to fabricate FPI with the same cavity length at room temperature, each FPI should be calibrated separately before it can be used for the temperature measurement.

The calibration process of FPI is discussed briefly in the previous chapter. FPI sensor together with a thermal coupler is placed inside a furnace, while temperature information and cavity length of the FPI is recorded simultaneously by the thermal coupler and computer. The furnace can be programmed so temperature increase or decrease speed is slow to guarantee enough response time for the FPI. Another way of calibration is to program the furnace to change the temperature in step manner and record temperature and cavity length for each step. By each of the above methods, we can get cavity length as function of temperature and draw the calibration curve. In actual temperature measurements with FPI, extracted cavity length is used to compare with the calibration curve to obtain temperature. Accuracy of the FPI is determined by both sensor quality and accuracy of the thermal coupler that is used for calibration. Thermal coupler can be replaced by other thermal meters when higher resolution and accuracy of

temperature measurement is required. Usually it is convenient to use the step method for calibration and fit the data with a polynomial function to obtain calibration curve on full measurement range. It is a time saving method for calibration, but the accuracy is relatively low. Figure 9-1 shows the calibration plot obtained by the above method. The black curve shows the extracted cavity length for fixed temperature, while the red curve shows polynomial fitting results which will be used as the calibration data.

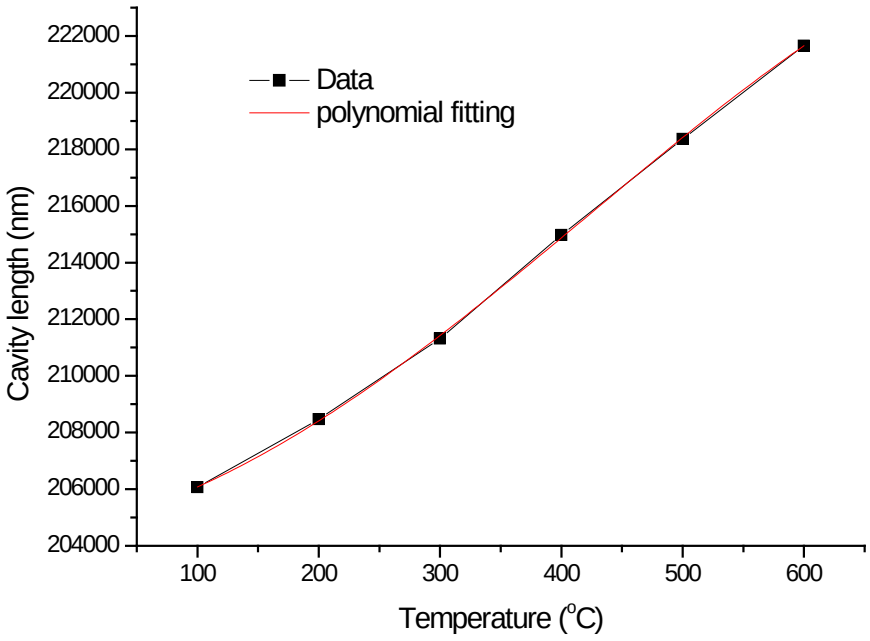

Figure 9-1: Polynomial fitting for calibration

To get high accuracy measurements, it is better to record continuous calibration curve with low temperature change speed, or actually record the temperature and real time cavity length simultaneously, which is shown in Figure 9-2.

The response time of the FPI sensor is important for this method, which depends on both the material and cavity design. In most situations, the response time of FPI is fast

enough for temperature measurement, but for accuracy purpose, longer calibration time is better.

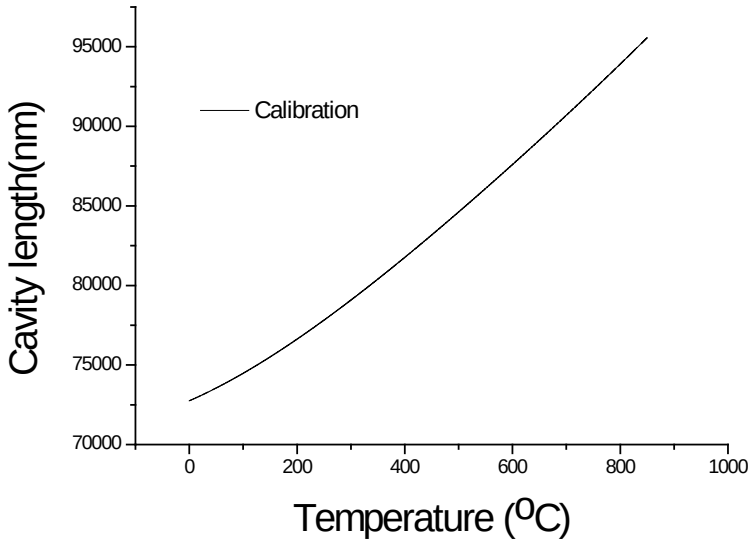

Figure 9-2: Simultaneously recording cavity length with temperature

9.2 Sensor stability

The stability of sensors at extreme condition is important, especially in this project while temperature sensor is used continuously for a long time in high temperature conditions. The sensor is placed in a furnace at 758 ^{o}C for more than 50 days. Cavity length and corresponding temperature is recorded. Figure 9-3 shows recorded data as a function of time.

An obvious shift is observed in Figure 9-3. Cavity length shifts from around 152290 nm to 152120 nm after 50 days. The shift speed is about 3nm/day. Related temperature shows a total of about 5 ^{o}C shift. The average shift speed for temperature is 0.1^{o}C/day. Shift of cavity length has near linear relationship, and no obvious change of slope is observed after 50 days. It should be noticed that the temperature for this measurement is 758 ^{o}C, which is close to the upper limit of our FPI design.

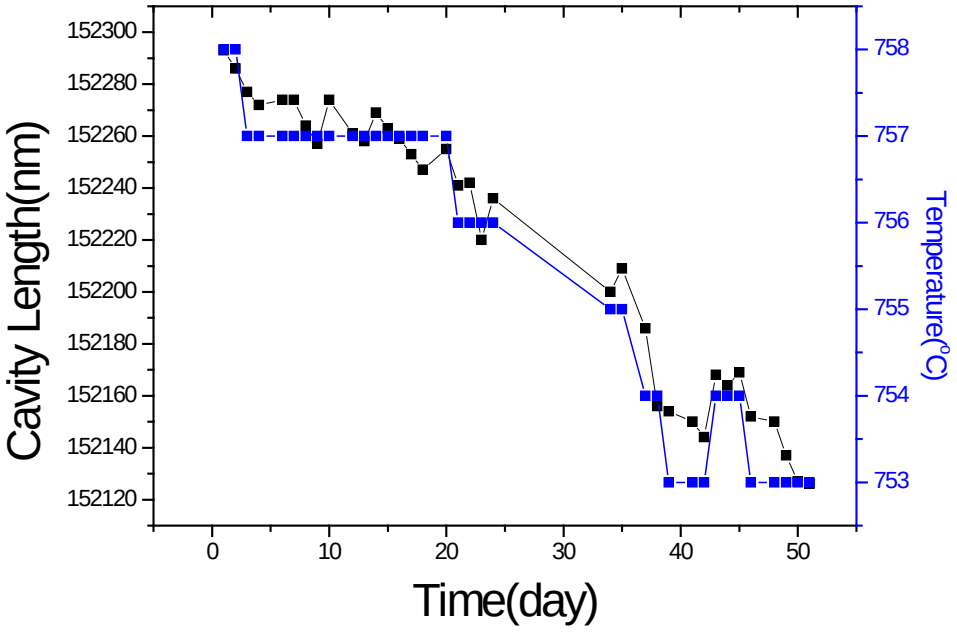

Figure 9-3: Long time stability measurement

The temperature inside the furnace is confirmed with a thermal coupler. After 50 days, temperature change read by the thermal coupler is less than 1 ^{o}C. So the drift problem is not coming from environment. Continuous decrease of cavity length indicates that it is not random fluctuation. Possible reasons for this drift could be the crystallization of the ceramic tube or fiber. Constitution of ceramic tube is 99.8% alumina with less than 0.07% Silica and other materials, which should be quite stable. It is difficult to evaluate the crystallization of ceramic tube or glass fiber, but we do notice that after long time annealing silica fiber becomes more fragile which means the structure and possible length changes.

9.3 Sensor specification

With optimized sensor fabrication and improved data processing technique, we finally achieve the best design for our FPI temperature sensor. The table below shows the sensor specification.

Table 9-1: Specification of sensor

Sensor specification	value
Materials	Silica fiber, Ceramic tube, Ceramic glue
Size	1 mm (diameter)*5 mm (length)
Temperature resolution	0.01 ^{o}C
Measurement range	Room temperature - 850 ^{o}C
Hysteresis	Less than 1 ^{o}C
Accuracy	Better than 1 ^{o}C
Temperature drift	0.1 ^{o}C/day at 758 ^{o}C

Based on the above specification, our sensor is perfect for use in harsh environments for temperature measurement lower than 850 ^{o}C. Due to the small size of the sensor, it is possible to measure temperature with high spatial resolution in a small area. Compared with reports from other groups on FPI sensors which usually show deviation of cavity length larger than 2nm (0.3 ^{o}C) [15] for FFT method, or experiences abrupt cavity length "jump" for non-FFT method, our temperature resolution can reach as high as 0.2 nm (0.01 ^{o}C) without an ambiguity problem. This method actually enables real time temperature measurement with high resolution and reliability. Besides, the additional annealing process provides less hysteresis compared with other groups [15, 39], which

greatly improves the accuracy of FPI based sensors. Compared with traditional temperature sensors, our sensors are more stable and robust in the chemical environment.

9.4 Multiple sensor system

Optical temperature measurement system can be built up based on theFPI sensor. The main components of this system include the light source, fiber coupler, FPI sensor probe and spectrometer.

The broadband light source and spectrometer is not cost-efficient selection. But for high accuracy temperature measurement, it is necessary to have a full spectrum acquisition and processing system. To reduce the cost, the in-line multiple sensor system has been proposed and demonstrated [15, 33]. In this design, FPI probes are connected in series so multiple point detection is enabled with reduced cost. On the other hand, the disadvantage of this geometry is obvious. First, the complex data processing techniques are required. The spectrum acquired by spectrometer will be a combination of the reflected light from multiple FPI sensors. Additional steps are required to separate them for cavity length extraction. Although the FFT technique can be used for this purpose, the cavity lengths of these FPI have to be significantly different so the FFT peak can be fully separated. Otherwise the data processing technique cannot guarantee accurate extraction of cavity length. Another problem for this geometry is the stability. Although the FPI sensors can be fabricated with high stability, the damage of FPI sensors still happens during the temperature measurement. For the in-line geometry, damage of one FPI might cause signal loss for other FPIs. Also, the in-line system introduces more difficulty on sensor fabrication process.

Based on the above consideration, in-line geometry is abandoned. We proposed another option for the multiple sensor system, which is based on a parallel FPI design. In this geometry, an additional instrument is required to connect multiple FPI sensors in parallel. In our system, we use a 16-channel optical switch. The optical switch is connected to the light source and spectrometer by the fiber coupler, while multiple FPI sensors are connected onto each channel of the optical switch. The left image of the Figure 9-4 shows a schematic drawing of the system. The purpose of this design is to reduce the cost of system by control of multiple FPI sensors. The maximum number of sensors is limited by the number of channels on the optical switch. Also because the connection is parallel for each sensor, the spectrometer will only acquire lights from one FPI at a time, which means the additional data processing technique to separate light from each FPI is not required. And any damages on one FPI will not affect others.

Despite the advantages mentioned above, adding an optical switch actually increases the total cost of the whole system. However, the average cost for each sensor is reduced.

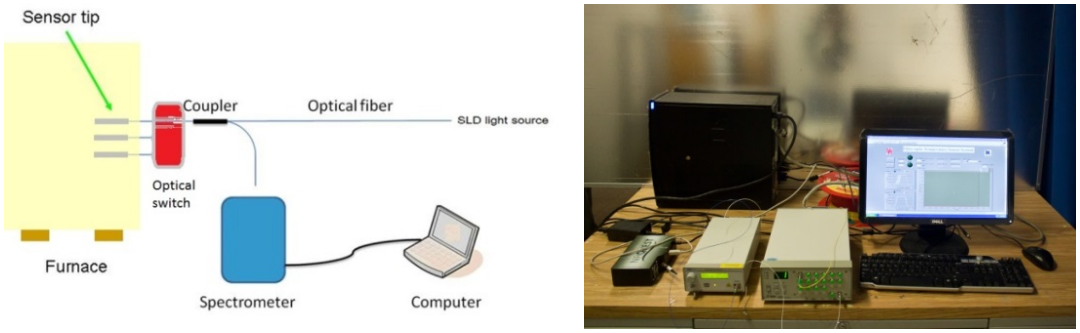

Figure 9-4: multiple FPI system, schematic and real system

The right hand image in Figure 9-4 shows a real multiple sensor system. Two FPI as demonstration have been connected to the optical switch, while a simultaneous temperature measurement is obtained.

Figure 9-5 shows the flow chart of software technique to obtain the absolute cavity length. This technique makes use of the existing functions provided by LabView so that software development time can be reduced. The speed of processing is mainly limited by the spectrum acquisition time, typically 100 ms.

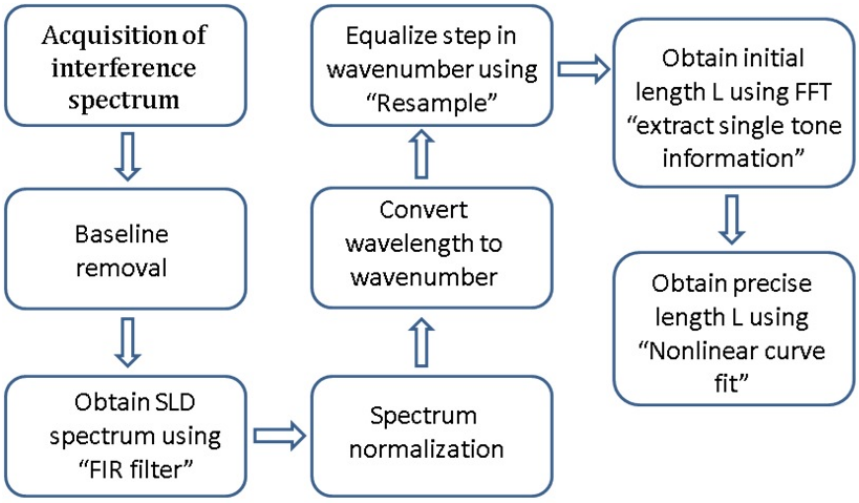

Figure 9-5: Flow chart used to calculate the absolute cavity length using revised non-linear curve fitting and LabView internal functions

For multiple sensor measurement, full control on optical switch and spectrometer is required. Figure 9-6 shows the front panel of software that we programmed for double FPI measurement system as demonstration. The measurement of each sensor can be separately controlled, while the cavity length as well as temperature can be recorded.

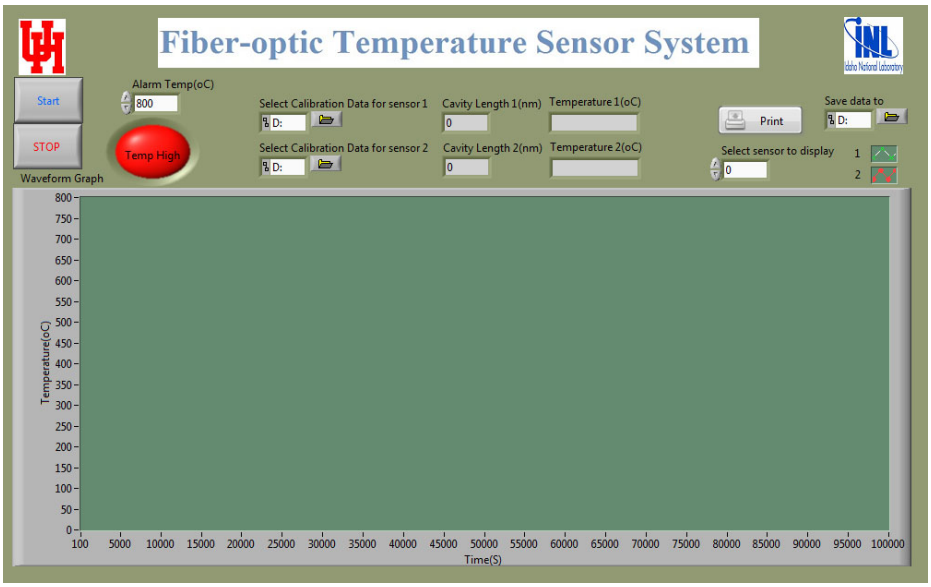

Figure 9-6: Data processing flow wavenumber fitting method

Chapter 10: Summary and conclusion

To develop a robust and high resolution temperature sensor with a large measurement range that is capable of real time temperature recording, comprehensive study on theory, sensor design, fabrication and optimization, novel data processing development, sensor performance, simulation and visibility control, additional phase term discussion, multiple sensor system development and long-time stability measurement are presented. This chapter gives summarization on achievements and conclusion of this research.

1. Optimization of sensor fabrication process to improve sensor performance

Hysteresis of FPI sensor, observed as temperature measurement difference between heating and cooling, is studied. Possible cause of hysteresis is discussed and addressed. Careful examination and analysis indicates that the hysteresis can be attributed to the ceramic glue that is used to bond the sensor, which could give out vapor during annealing. Although the above hypothesis is not confirmed, by adding annealing steps before the cavity is built hysteresis can be reduced. Sensor performance before and after optimization is compared, while significant improvement is obtained.

2. Control of visibility during fabrication

Visibility can be used to represent the quality of FPI. At the beginning, we achieved high visibility compared with reports [11] from other groups during sensor fabrication but we do nott have control on it. To fully understand and control the visibility, simulation is used to study the factors that affect visibility, which includes the cavity length and reflection coefficient of the cavity. Although glass fiber is used which means the reflection coefficient of the cavity is fixed, we realize that the effective reflection

coefficient of the cavity could be different, which is verified by direct measurement of reflected light from the fiber end and comparison of its intensity with light source. It turns out that effective reflection coefficient can be affected by the surface condition of the fiber end, which is determined in our case by the surface preparation method. To further demonstrate, control experiment is designed to fabricate FPI with a different effective reflection coefficient of the leading fiber. The experimental data match with simulation results, and the shift of peak position to larger cavity length on the visibility curve is observed in the predicted condition. Above results indicate that full control of sensor visibility in measurement range is possible by careful selection of surface preparation method.

3. Study on additional phase problem

The additional phase has been studied. A novel data processing technique is proposed to extract this term. The calculation results based on experimental data do not match perfectly with theoretical predictions from other groups, which indicates that either modification of the theoretical model is required, or other factors exist that can affect additional phase.

4. Sensor long term stability test under high temperature

Long term stability of temperature sensors is important. To verify this feature, our FPI sensor is placed in a furnace at 758 ^{o}C for 50 days. The temperature is very close to the measurement limit of our sensor. After 50 days, around 170 nm cavity length drift is observed which corresponds to a drift speed of 0.1 ^{o}C / day. Considering the extreme condition for this test, the drift is acceptable in our application.

5. Novel data processing technique for absolute cavity length extraction

A novel data processing technique has been proposed in this dissertation. It combines the FFT method and curve fitting technique for the extraction of cavity length. FFT method is used to obtain cavity length with a large fluctuation as a fitting parameter. The FFT technique has relatively low temperature resolution, with standard cavity length deviation of around 10s nm, which corresponds to around 0.7 ^{o}C. On the other hand, the curve fitting method can provide high temperature resolution. The standard cavity length deviation for this method is less than 0.5nm, which corresponds to around 0.015 ^{o}C. But there exists cavity length ambiguity problem for this method, which could cause a cavity length jump. By a combination of these two methods, the new technique can provide high resolution of temperature measurement without the ambiguity problem.

6. Multiple sensor system

A parallel FPI sensor system is proposed in this dissertation to reduce cost. The maximum number of FPI that can be used in this system is solely limited by the number of channels of the optical switch. Software that is used to control optical switch and the spectrometer for data acquisition and processing for each sensor is programmed. For demonstration purposes, two FPI are connected to the system and simultaneously read out of temperature information from both sensors are achieved.

Reference

[1] Z. Zhang, K. T. V. Grattan, and A. W. Palmer, "Fiber optic temperature sensor based on the cross referencing between blackbody radiation and fluorescence lifetime," *Review of Scientific Instruments*, vol. 63, p. 3177, 1992.

[2] M. A. Soto, T. Nannipieri, A. Signorini, A. Lazzeri, F. Baronti, R. Roncella, *et al.*, "Raman-based distributed temperature sensor with 1 m spatial resolution over 26 km SMF using low-repetition-rate cyclic pulse coding," *Opt Lett*, vol. 36, pp. 2557-9, Jul 1 2011.

[3] D. V. Nelson, A. Makino, C. M. Lawrence, J. M. Seim, W. L. Schulz, and E. Udd, "Determination of the K-matrix for the multiparameter fiber grating sensor in AD072 fibercore fiber," in *Pacific Northwest Fiber Optic Sensor Workshop*, 1998, pp. 79-85.

[4] E. J. Lang and T.-W. Chou, "The effect of strain gage size on measurement errors in textile composite materials," *Composites science and technology*, vol. 58, pp. 539-548, 1998.

[5] E. Udd, W. L. Schulz, J. M. Seim, E. D. Haugse, A. Trego, P. E. Johnson, *et al.*, "Multidimensional strain field measurements using fiber optic grating sensors," in *SPIE's 7th Annual International Symposium on Smart Structures and Materials*, 2000, pp. 254-262.

[6] W. L. Schulz, E. Udd, J. M. Seim, I. M. Perez, and A. Trego, "Progress on monitoring of adhesive joints using multiaxis fiber grating sensors," in *SPIE's 7th Annual International Symposium on Smart Structures and Materials*, 2000, pp. 52-61.

[7] L. Song, Z. Wang, A. Wang, Y. Liu, and K. L. Cooper, "Angular dependence of the frequency response of an extrinsic Fabry-Perot interferometric (EFPI) fiber acoustic sensor for partial discharge detection," *Journal of lightwave technology*, vol. 24, p. 3433, 2006.

[8] N. Fürstenau, M. Schmidt, H. Horack, W. Goetze, and W. Schmidt, "Extrinsic Fabry–Perot interferometer vibration and acoustic sensor systems for airport ground traffic monitoring," *IEE Proceedings-Optoelectronics*, vol. 144, pp. 134-144, 1997.

[9] J. J. Zhu, A. Zhang, T. H. Xia, S. He, and W. Xue, "Fiber-optic high-temperature sensor based on thin-core fiber modal interferometer," *Sensors Journal, IEEE*, vol. 10, pp. 1415-1418, 2010.

[10] H. S. Choi, H. F. Taylor, and C. E. Lee, "High performance fiber optic temperature sensor using low-coherence interferometry," in *Optical Fiber Sensors*, 1997.

[11] X. Chen, F. Shen, Z. Wang, Z. Huang, and A. Wang, "Micro-air-gap based intrinsic Fabry-Perot interferometric fiber-optic sensor," *Applied optics*, vol. 45, pp. 7760-7766, 2006.

[12] H. Y. Choi, K. S. Park, S. J. Park, U.-C. Paek, B. H. Lee, and E. S. Choi, "Miniature fiber-optic high temperature sensor based on a hybrid structured Fabry–Perot interferometer," *Optics letters*, vol. 33, pp. 2455-2457, 2008.

[13] J. l. Kou, J. Feng, L. Ye, F. Xu, and Y. q. Lu, "Miniaturized fiber taper reflective interferometer for high temperature measurement," *Opt. Express*, vol. 18, pp. 14245-14250, 2010.

[14] Y. Chen and H. F. Taylor, "Multiplexed fiber Fabry–Perot temperature sensor system using white-light interferometry," *Optics letters*, vol. 27, pp. 903-905, 2002.

[15] J. Wang, B. Dong, E. Lally, J. Gong, M. Han, and A. Wang, "Multiplexed high temperature sensing with sapphire fiber air gap-based extrinsic Fabry–Perot interferometers," *Optics letters*, vol. 35, pp. 619-621, 2010.

[16] T. Li, R. G. May, A. Wang, and R. O. Claus, "Optical scanning extrinsic Fabry-Perot interferometer for absolute microdisplacement measurement," *Applied optics*, vol. 36, pp. 8858-8861, 1997.

[17] K. A. Murphy, M. F. Gunther, A. M. Vengsarkar, and R. O. Claus, "Quadrature phase-shifted, extrinsic Fabry-Perot optical fiber sensors," *Optics Letters*, vol. 16, pp. 273-275, 1991.

[18] A. Wang, S. Gollapudi, R. G. May, K. A. Murphy, and R. O. Claus, "Sapphire optical fiber-based interferometer for high temperature environmental applications," *Smart Materials and Structures*, vol. 4, p. 147, 1995.

[19] Y. Zhu, Z. Huang, F. Shen, and A. Wang, "Sapphire-fiber-based white-light interferometric sensor for high-temperature measurements," *Optics letters*, vol. 30, pp. 711-713, 2005.

[20] A. Wang, H. Xiao, J. Wang, Z. Wang, W. Zhao, and R. G. May, "Self-calibrated interferometric-intensity-based optical fiber sensors," *Journal of lightwave technology*, vol. 19, p. 1495, 2001.

[21] H. Xiao, J. Deng, G. Pickrell, R. G. May, and A. Wang, "Single-crystal sapphire fiber-based strain sensor for high-temperature applications," *Journal of lightwave technology*, vol. 21, p. 2276, 2003.

[22] A. Wang, M. S. Miller, A. J. Plante, M. F. Gunther, K. A. Murphy, and R. O. Claus, "Split-spectrum intensity-based optical fiber sensors for measurement of

microdisplacement, strain, and pressure," *Applied optics*, vol. 35, pp. 2595-2601, 1996.

[23] Y. Zhu and A. Wang, "Surface-mount sapphire interferometric temperature sensor," *Applied optics*, vol. 45, pp. 6071-6076, 2006.

[24] C. E. Lee and H. F. Taylor, "Fiber-optic Fabry-Perot temperature sensor using a low-coherence light source," *Lightwave Technology, Journal of*, vol. 9, pp. 129-134, 1991.

[25] L. V. Nguyen, D. Hwang, S. Moon, D. S. Moon, and Y. Chung, "High temperature fiber sensor with high sensitivity based on core diameter mismatch," *Opt. Express*, vol. 16, pp. 11369-11375, 2008.

[26] C. Zhan, J. H. Kim, J. Lee, S. Yin, P. Ruffin, and C. Luo, "High temperature sensing using higher-order-mode rejected sapphire-crystal fiber gratings," in *Proc. SPIE*, 2007, p. 66980F.

[27] S. H. Nam, C. Zhun, and S. Yin, "Recent advances on fabricating in-fiber gratings in single crystal sapphire fiber," in *Proc. SPIE*, 2004, pp. 147-155.

[28] D. Monzon-Hernandez, V. P. Minkovich, and J. Villatoro, "High-temperature sensing with tapers made of microstructured optical fiber," *Photonics Technology Letters, IEEE*, vol. 18, pp. 511-513, 2006.

[29] D. Jackson, "Recent progress in monomode fibre-optic sensors," *Measurement Science and Technology*, vol. 5, p. 621, 1994.

[30] H. Xiao, J. Deng, Z. Wang, W. Huo, P. Zhang, M. Luo, *et al.*, "Fiber optic pressure sensor with self-compensation capability for harsh environment applications," *Optical Engineering*, vol. 44, pp. 054403-054403-10, 2005.

[31] V. Machavaram, R. Badcock, and G. Fernando, "Fabrication of intrinsic fibre Fabry–Perot sensors in silica fibres using hydrofluoric acid etching," *Sensors and Actuators A: Physical*, vol. 138, pp. 248-260, 2007.

[32] T. Liu, G. Fernando, Z. Zhang, and K. Grattan, "Simultaneous strain and temperature measurements in composites using extrinsic Fabry–Perot interferometric and intrinsic rare-earth doped fiber sensors," *Sensors and Actuators A: Physical*, vol. 80, pp. 208-215, 2000.

[33] Y. Zhang, X. Chen, Y. Wang, K. L. Cooper, and A. Wang, "Microgap Multicavity Fabry–Pérot Biosensor," *Journal of lightwave technology*, vol. 25, pp. 1797-1804, 2007.

[34] F. Shen and A. Wang, "Frequency-estimation-based signal-processing algorithm for white-light optical fiber Fabry-Perot interferometers," *Applied optics*, vol. 44, pp. 5206-5214, 2005.

[35] Y. Ning, K. Grattan, and A. Palmer, "Fibre-optic interferometric systems using low-coherence light sources," *Sensors and Actuators A: Physical*, vol. 30, pp. 181-192, 1992.

[36] M. Born and E. Wolf, *Principles of optics: electromagnetic theory of propagation, interference and diffraction of light*: CUP Archive, 1999.

[37] M. Han, Y. Zhang, F. Shen, G. R. Pickrell, and A. Wang, "Signal-processing algorithm for white-light optical fiber extrinsic Fabry-Perot interferometric sensors," *Optics letters*, vol. 29, pp. 1736-1738, 2004.

[38] C. Ma, B. Dong, J. Gong, and A. Wang, "Decoding the spectra of low-finesse extrinsic optical fiber Fabry-Perot interferometers," *Optics Express*, vol. 19, pp. 23727-23742, 2011.

[39] J. Wang, E. M. Lally, B. Dong, J. Gong, and A. Wang, "Fabrication of a miniaturized thin-film temperature sensor on a sapphire fiber tip," *Sensors Journal, IEEE,* vol. 11, pp. 3406-3408, 2011.